

## PORT DOCUMENTATION PAGE

AD-A213 740

10. RESTRICTIVE MARKINGS

THE FILE COPY

3. DISTRIBUTION/AVAILABILITY OF REPORT

Approved for public release,  
distribution unlimited

4. PERFORMING ORGANIZATION REPORT NUMBER(S)

5. MONITORING ORGANIZATION REPORT NUMBER(S)

AFOSR-TR- 89-1150

6a. NAME OF PERFORMING ORGANIZATION  
The Regents of the University  
of California6b. OFFICE SYMBOL  
(If applicable)7a. NAME OF MONITORING ORGANIZATION  
Dr. C. Lee Giles  
AFOSR/NE

6c. ADDRESS (City, State and ZIP Code)

University of California, San Diego  
La Jolla, CA, 92093-0407

7b. ADDRESS (City, State and ZIP Code)

AFOSR/NE, Bolling Air Force Base  
Washington, D. C. 203328a. NAME OF FUNDING/SPONSORING  
ORGANIZATION8b. OFFICE SYMBOL  
(If applicable)9. PROCUREMENT INSTRUMENT IDENTIFICATION NUMBER  
AFOSR-84-0389

8c. ADDRESS (City, State and ZIP Code)

AFOSR/PKD  
Building 410  
Bolling AFB D.C., 203320-6448

10. SOURCE OF FUNDING NOS.

PROGRAM  
ELEMENT NO.PROJECT  
NO.TASK  
NO.WORK UNIT  
NO.

11. TITLE (Include Security Classification)

Research of Materials and Components for Opto-  
electronic Signal Processing and Computing

12. PERSONAL AUTHOR(S)

William S.C. Chang, Timothy Van Eck, Shigeru Niki, Andrew Williams, Albert L. Kellner and  
H. H. Wieder

13a. TYPE OF REPORT

Final Scientific

13b. TIME COVERED

FROM 10/1/84 TO 11/30/88

14. DATE OF REPORT (Yr., Mo., Day)

July 20, 1989

15. PAGE COUNT

77

16. SUPPLEMENTARY NOTATION

17. COSATI CODES

FIELD

GROUP

SUB. GR.

18. SUBJECT TERMS (Continue on reverse if necessary and identify by block number)

19. ABSTRACT (Continue on reverse if necessary and identify by block number)

Electro-absorption and electro-refraction properties of heterostructures and multiple quantum-well structures in GaInAs/GaAs were demonstrated and optimized for spatial light modulation applications. Techniques to generate and to confine dislocations near the substrate interface to grow a large number of strained quantum wells have been developed. Modulation at 1.06  $\mu\text{m}$  wavelength were observed using strained layer quantum wells. Optical-optical interaction in a multiple quantum well detector modulator pair has been demonstrated. A new device, the gate controlled photo-diode has been conceived and demonstrated.

20. DISTRIBUTION/AVAILABILITY OF ABSTRACT

UNCLASSIFIED/UNLIMITED ☒ SAME AS RPT. ☐ DTIC USERS ☐

21. ABSTRACT SECURITY CLASSIFICATION

Unclassified

22a. NAME OF RESPONSIBLE INDIVIDUAL

Dr. C. Lee Giles

22b. TELEPHONE NUMBER

(Include Area Code)  
(202)767-4931

22c. OFFICE SYMBOL

NE

**AFOBR-TR- 89-1150**

**Final Scientific Report**

**Research on Materials and Components for  
Opto-Electronic Signal Processing and Computing**



**Sponsored by**

**Air Force Office of Scientific Research  
Air Force Systems Command, USAF**

**under Grant No. 84-0389  
From October 1st, 1984 to November 30, 1988**

**submitted by**

**William S. C. Chang (Principal Investigator)  
Timothy Van Eck, Shigeru Niki, Andrew Williams,  
Albert L. Kellner and H. H. Wieder**

Accession For	
NTIS	<input checked="" type="checkbox"/>
DTIC	<input type="checkbox"/>
Unannounced	<input type="checkbox"/>
Justification	
By	
Distribution	
Availability Codes	
Dist	
Special	

**A-1**

**Department of Electrical and Computer Engineering, R-007  
University of California, San Diego  
La Jolla, CA, 92093  
Tel. (619) 534-2737**

**The United States Government is authorized to reproduce and  
distribute reprints for Government purposes not withstanding  
any copyright notation thereon.**

## RESEARCH ON MATERIALS AND COMPONENTS FOR OPTO-ELECTRONIC SIGNAL PROCESSING AND COMPUTING

### 1. INTRODUCTION

It has been recognized for sometime that optical signal processing holds considerable promise for high speed signal processing in DoD applications. For example optical computing, neural-network and optical fiber communications are some of the current military research interests. However, characteristics of the materials and components (including microfabrication processing technology) must be improved substantially before the full potential of combined opto-electronic signal processing can be realized.

In III-V compound semiconductors, optical devices such as lasers and detectors have already been realized and used in many applications. High speed electronic devices such as the GaAs MESFET, the HEMT and the HBT have also been demonstrated. Electronic and optical devices may potentially be integrated monolithically on the same chip. The advantages of integrated opto-electronic signal processing include high speed of operation, parallel processing, versatility, capability for complex interconnections and reliability and convenience of optical-electronic signal conversion. Recent advancements in the research of heterojunctions, quantum well and superlattice III-V compound semiconductor structures have already demonstrated unique electronic and optical properties such as high mobility in modulation doped structures, large nonlinear optical effect and sharp tunable exciton lines at room temperature. The heterojunction, quantum well and superlattice structures of these materials offer many potentially exciting "material engineering" opportunities, critically needed for the development of novel components. If there is a material and device technology that may catalyze the future advancements in high-speed optical/electronic technology with far reaching consequences such as silicon had done for microelectronics, it is the technology based on III-V semiconductors and related ternary and quaternary alloys.

The electronic and optical properties of some semiconductor MQW's can be designed for specific applications by changing the effective thickness of the III-V compound semiconductor layers and the alloy composition of the heterojunction structures which make up such MQW's. Additional flexibility is available in varying these properties and can be obtained by accommodating lattice-mismatched layers by the introduction of uniform layer strains so that no misfit dislocations are generated at the MQW interfaces. Strained layer (SL) MQW's have a lattice constants parallel to the MQW interface,  $\alpha'$ , which is a strong function of the layer structure, the layer thickness, the elastic constants and the shear moduli of the alloys <sup>[1]</sup>. It is, in fact, possible to vary the composition of the MQW and the layer thickness while keeping  $\alpha'$  fixed and this suggests the possibility of varying, correspondingly, a number of electronic, optical and electro-optic properties, including the fundamental bandgap  $E_g$ . The  $\text{In}_x\text{Ga}_{1-x}\text{As}/\text{GaAs}$  SL structure is of particular interest because  $\text{In}_x\text{Ga}_{1-x}\text{As}$  encompasses a wide range of  $E_g$ , from that of InAs,  $E_g = 0.36$  eV to that of GaAs,  $E_g = 1.42$  eV at room temperatures. It is of interest for spatial light modulator applications because the GaAs substrate used to grow the MQW is transparent for  $x > 0$  in the vicinity of  $E_g$  of the  $\text{In}_x\text{Ga}_{1-x}\text{As}$  MQW. In contrast, the GaAs substrate of the  $\text{Al}_y\text{Ga}_{1-y}\text{As}/\text{GaAs}$  MQW structures must be etched away for spatial light modulation in order to avoid substrate attenuation. Moreover the silicon doping of  $\text{Al}_y\text{Ga}_{1-y}\text{As}$  introduces deep level traps, particularly for  $y > 0.2$  and these traps are responsible for the persistent photoconductive effects at low temperatures. These centers may affect the speed of spatial modulation. To first order there seem to be no such problems with the  $\text{In}_x\text{Ga}_{1-x}\text{As}/\text{GaAs}$  system.

During the period of this research grant we have focused our effort on the investigation of  $\text{In}_x\text{Ga}_{1-x}\text{As}/\text{GaAs}$  multiple quantum well (MQW) strained layer (SL) structures grown by the molecular beam epitaxy (MBE) method for spatial light modulation (SLM) applications. In the beginning of the grant period a Gate Controlled Photo Diode was also investigated. This investigation was terminated on July 1st, 1986. Nevertheless it constituted the Ph.D. Thesis of C. C. Sun. A paper entitled "A New Semiconductor Device -The Gate-Controlled Photodiode:

Device Concept and Experimental Results" was accepted for publication by the IEEE Journal of Quantum Electronics. Since we will not be discussing the technical detail of that work in this report, a preprint of that paper is attached here as Appendix A.

In the following paragraphs, we will summarize our results in (a) The electro-absorption (EA) and electrorefraction (ER) of the  $\text{In}_x\text{Ga}_{1-x}\text{As}/\text{GaAs}$  SL MQW materials grown in our MBE. (b) The optimization of EA as a function of quantum well thickness and indium composition. (c) A material growth technique developed at UCSD to obtain large number of quantum wells with relatively large indium concentration and without creating many dislocations. (d) The extension of the strained layer technology to obtain EA at the  $1.06\text{ }\mu\text{m}$  wavelength where the powerful Nd/YAG laser operates. (e) The automation of the MBE growth by computer control for fabrication of complex structures. (f) Design and fabrication of SLM structures with large modulation depth and low operating voltage, (g) Demonstration of the detector-modulator pair.

The two most important results are: (1) Demonstration of the sharp electroabsorption spectra in the MQW  $\text{In}_x\text{Ga}_{1-x}\text{As}/\text{GaAs}$  SL structures. (2) Techniques to generate and to confine dislocations near the substrate interface so a large number of SL quantum wells may be grown. In this case the quantum wells have a slightly different lattice constant than the substrate. Numerous other tasks were also accomplished in the process, but they are not discussed in the summary of results. Some of them have been done in collaboration with other research project at UCSD. They include: (1) Development of the photo-luminescence set-up to evaluate the exciton spectra. (2) Extension of a commercial argon laser pumped C.W. dye laser into the  $0.92$  to  $0.97\text{ }\mu\text{m}$  wavelength range for evaluation. (3) Development of the thick plating of gold electrode for wire bonding that will not damage the quantum wells below. (4) Computer data collection schemes for EA and ER measurement using the pulsed dye laser-parametric oscillator as the source. Collaboration with Lockheed Missile and Space Company is crucial in obtaining the TEM cross sectional micrographs of the quantum well and superlattice buffer structures.

## 2. ELECTRO-ABSORPTION (EA) AND ELECTRO-REFRACTION (ER)

$\text{In}_x\text{Ga}_{1-x}\text{As}/\text{GaAs}$  MQW's using such SL structures were grown by molecular beam epitaxy (MBE) on GaAs substrates by Fritz et al. [2,3] with layer thicknesses in the 40 Å to 140 Å range. A confirmation of the effects of strain and layer thickness of SL  $\text{In}_x\text{Ga}_{1-x}\text{As}/\text{GaAs}$  MQW was provided by Laidig et al. [4] using  $x \approx 0.38$  and  $x \approx 0.28$ . However, they found from X-ray diffraction analysis, a substantial broadening of diffracted peaks of thick layers estimated to be between 770 Å and 470 Å in thickness, particularly for large values of  $x$ , while for layer thicknesses between 96 Å and 56 Å, the diffraction peaks remain sharp and scanning electron microscopy confirmed, furthermore, that the broadening of the X-ray peaks is accompanied by the presence of structural defects produced by strain relief in the thicker layers.

During the FY86, strained layer  $\text{In}_x\text{Ga}_{1-x}\text{As}$  MQW's were grown at UCSD on n-doped and p-doped (100)-oriented GaAs substrates by means of MBE. The In mole fraction  $x$  was restricted to  $x = 0.13$  and  $x = 0.15$  thus producing alloy layers with pseudomorphic, tetragonally distorted interfaces. Ten layer MQW's were grown at 530°C on an initial 0.3 μm thick GaAs undoped buffer layer followed by ten alternating 10 nm thick  $\text{In}_x\text{Ga}_{1-x}\text{As}$  layers and 15 nm thick GaAs layers with and without a GaAs capping layer.

Assuming that the fundamental bandgap at room temperature of the unstrained ternary alloy system  $\text{In}_x\text{Ga}_{1-x}\text{As}$  is represented by

$$E_g = 1.42 - 1.615x + 0.555x^2$$

then for  $x = 0.15$ ,  $E_g = 1.19$  eV and  $\Delta E_g = 0.23$  eV. By including the correction for the compressive strain on  $E_g(\text{In}_x\text{Ga}_{1-x}\text{As})$  we estimate  $\Delta E_g = 0.173$  eV, the conduction band discontinuity to be of the order  $\Delta E_c = 0.13$  eV and the valence band discontinuity to be  $\Delta E_v = 0.06$  eV. In spite of these relatively low band edge discontinuities we have reported the observation of sharp exciton absorption and effective EA as a function of externally applied bias voltage at room temperature on p-i-n diodes made of the 10 layers of  $\text{In}_{0.13}\text{Ga}_{0.87}\text{As}$  MQW<sup>[5,6]</sup>, Figure 1 shows the electro-absorption spectra of Sample MBE-110. We have also reported the large ER effect on a sample supplied to us by the MIT Lincoln Laboratory<sup>[7]</sup>. Figure 2 shows the

electro-refraction spectra. These results indicated the large potential of  $\text{In}_x\text{Ga}_{1-x}\text{As}/\text{GaAs}$  QW structures in achieving high speed and low switching voltage spatial light modulation.

### 3. QUANTUM WELL OPTIMIZATION

The EA spectrum of a QW consists essentially of a sharp peak, a plateau on the high-energy side of the peak and no absorption on the low-energy side. The peak corresponds to exciton absorption, and the plateau corresponds to sub-band continuum absorption. When an electric field is applied perpendicular to the QW's, both the exciton peak and the associated continuum shift to lower energy, lose strength, and are broadened. If the incident light is tuned to the wavelength of the exciton peak in the absence of the electric field, then the absorption of the structure is reduced, and negative EA is obtained. If the incident light is tuned to the wavelength of the field-shifted exciton peak, then the electric field increases the absorption, and positive EA results. Some applications require positive electro-absorption (e.g. SEED self-linearized modulation) and some require negative electro-absorption (e.g. SEED switching). Positive electro-absorption will provide a smaller insertion loss, since absorption is very small in the OFF condition, but negative electro-absorption seems to provide a larger modulation depth.

The magnitude of the electro-absorption is determined by the following factors. These factors are illustrated in Figure 3.

1. The magnitude of the absorption at the peak (e.g. A or B in Figure 3). Since the area under the exciton line is proportional to the oscillator strength  $f$ , it will be proportional to  $f$  and inversely proportional to line width. The line width is proportional to the broadening parameter  $\Gamma$ .
2. The peak shift  $\Delta E$  caused by an applied voltage  $V$ .
3. The change of oscillator strength caused by an applied voltage,  $\Delta f(V)$ .
4. The change of broadening parameter  $\Delta \Gamma$  caused by an applied voltage.

An investigation on how to optimize the  $\text{In}_x\text{Ga}_{1-x}\text{As}/\text{GaAs}$  MQW structure for EA modulation has been carried out. A theoretical analysis of the exciton wave function in an infinitely deep potential well for the QW in an electric field has been developed by Bastard et al.<sup>[8]</sup> and was extended by us. Bastard's 1-D variational model predicts that

$$\Delta E \propto (m_e + m_h)(FL_z)^2 L_z^2$$

$$\Delta f \propto (M_e + m_h)(FL_z)^2 L_z^4$$

where  $F$  is the applied electric field in the  $z$  direction in the well;  $L_z$  is the thickness of the QW in the  $z$  direction. If the electric field is uniformly distributed, then  $FL_z$  is the applied voltage per well. For finite potential wells, a theoretical model describing the electric field dependence of  $\Delta E$  and  $\Delta f$  has been developed by Dermot Coffey of the UCSD Physics Department<sup>[9]</sup>. We have used Coffey's computer program<sup>[10]</sup> to compare the theoretical calculated results with our experimental data and to predict the dependence of the electro-absorption on well thickness and depth. Our experimental data is collected from two sets of three samples grown by MBE. In one set of the three samples, each sample has ten  $\text{In}_{0.12}\text{Ga}_{0.88}\text{As}$  QW's grown on GaAs without superlattice buffer but each has a different quantum well thickness 50 Å, 70 Å and 100 Å. The second set is the same as the first except that the QW's have 17% In. For the first set the absorption peak of the 50 Å  $\text{In}_{0.12}\text{Ga}_{0.88}\text{As}$  QW's was obscured by the GaAs substrate absorption tail, so this sample provided no useful data. Table 1 shows the comparison of the experimental and theoretical data where  $\Delta E_c = \Delta E_v$  is assumed to be 100 meV for  $\text{In}_{0.17}\text{Ga}_{0.83}\text{As}/\text{GaAs}$  and 70 meV for  $\text{In}_{0.12}\text{Ga}_{0.88}\text{As}/\text{GaAs}$ . The agreement between the theoretical results and the experimental data is good.

For positive electro-absorption  $\Delta f$  should be as small as possible while  $\Delta E$  reaches one FWHM. Since

$$\Delta f/\Delta E \propto (m_e + m_h)L_z^2,$$

thinner quantum wells are expected to provide stronger positive electro-absorption than thicker ones. For those SLM applications in which very low insertion loss or very high extinction ratio



TABLE 1.  
Comparison of the theoretical and Experimental Data of  
Electro-Absorption of  $\text{In}_x\text{Ga}_{1-x}\text{As}/\text{GaAs}$  MQW Structures

$$12\% \text{ In}/\Delta E_c = \Delta E_v = 70 \text{ meV}$$

$\Delta E(\text{meV})$

Voltage	70 Å		100 Å	
	Exp.	Th.	Exp.	Th.
1	-1.4	-1.0	-2.7	-1.9
2	-4.2	-4.0	-8.0	-7.9
3	-7.0	-9.3	----	----

$\Delta f/f_0$

Voltage	70 Å		100 Å	
	Exp.	Th.	Exp.	Th.
1	-.13	-.07	-.28	-.19
2	-.30	-.26	-.50	-.56
3	-.48	-.51	----	----

$$17\% \text{ In}/\Delta E_c = \Delta E_v = 100 \text{ meV}$$

$\Delta E(\text{meV})$

Voltage	50 Å		70 Å		100 Å	
	Exp.	Th.	Exp.	Th.	Exp.	Th.
1	-1.0	-0.4	-0.6	-0.7	-0.7	-1.5
2	-3.1	-1.5	-2.6	-2.7	-3.7	-5.8
3	-5.4	-3.4	-6.4	-6.2	----	----
4	-7.4	-6.0	-12.1	-11.2	----	----
5	-9.4	-9.4	----	----	----	----

$\Delta f/f_0$

Voltage	50 Å		70 Å		100 Å	
	Exp.	Th.	Exp.	Th.	Exp.	Th.
1	-.04	-.02	-.04	-.04	-0.9	-.12
2	-.09	-.06	-.11	-.15	-.23	-.39
3	-.22	-.14	-.22	-.32	----	----
4	-.35	-.23	-.38	-.50	----	----
5	-.47	-.35	----	----	----	----

is required, positive EA is the preferred mechanism. On the other hand, examination of all the electro-absorption data suggests that, for SLM applications in which low insertion loss is not required, we should use the negative electro-absorption effect. It will give the largest depth of modulation at the lowest applied voltage. In that case we should use a large  $L_z$  to obtain a large  $\Delta f$  and a large  $\Delta E$ , while the voltage per well (i.e.,  $FL_z$ ) is kept constant. In general, wide  $L_z$  and shallow potential wells (i.e.,  $\Delta E_c$  and  $\Delta E_v$ ) are preferred for negative electro-absorption. How wide an  $L_z$  and how shallow a  $\Delta E_c$  (and  $\Delta E_v$ ) can be used depend on practical considerations. For example, shallower quantum wells could be achieved by reducing the In content in the well. Reducing the In content will also lead to a reduction in strain, thereby improving the quality of the grown layers. However, there will be increased absorption from the bandtail of the GaAs substrate due to the proximity of the exciton peak to the GaAs band edge. This is very undesirable. Table 2 summarizes the mechanisms by which changing the quantum well thickness, well depth and bandgap can significantly affect electro-absorption. In this table  $F$  is the electrical field strength,  $f$  is the oscillator strength,  $\Delta E_c$  and  $\Delta E_v$  are conduction and valence band discontinuity between the well and the barrier, and the "+" and the "-" signs indicate whether the EA effect is enhanced or reduced by the change of the parameter.

The work on the optimization of QW structures for EA is part of the Ph.D. thesis of Timothy Van Eck.

#### 4. MATERIAL GROWTH TECHNIQUE FOR STRAIN RELIEF IN QW LAYERS

For opto-electronic spatial light modulation it is important to obtain reasonably large depth of modulation for light transmitted normal through the sample. Hence it is desirable to increase the number of SL quantum well periods by at least a factor of five over the number of periods that we have already made, e.g. 80 to 100 periods. However, investigations<sup>[11, 12]</sup> of the critical thickness for single quantum wells with  $x = 0.28$  and strained layer superlattices with  $0.14 < x < 0.35$  (with an effective strain  $\epsilon = \Delta a/a$  smaller than 2.7%) indicate a strong degradation of heterostructure quality when the total thickness of all the quantum wells approaches the value of

the critical thickness  $L_c$ , for generating misfit dislocations.  $L_c$  has been theoretically derived by Matthews and Blakeslee<sup>[13]</sup>. These relations were confirmed recently by Anderson et al.<sup>[14]</sup> for the full composition range  $0.1 < x < 1$ .

Bedair et al.<sup>[15]</sup> have shown a method for reducing the density of threading dislocations originating at the GaAs epitaxial interfaces. They found that strained superlattice structures grown by MBE directly on the GaAs substrate tend to localize the dislocation network and reduce the etch pit count by nearly two orders of magnitude. We have initiated work on the ternary alloy  $\text{In}_x\text{Al}_{1-x}\text{As}$  grown on GaAs for different purposes, concerned mainly with application of MODFET structures. We have been interested in the use of an  $\text{In}_x\text{Al}_{1-x}\text{As}$  buffer layer to reduce the dislocation densities of the MQW layers. With reference to Figure 4 note that for each  $\text{In}_x\text{Ga}_{1-x}\text{As}$  alloy there is a corresponding  $\text{In}_x\text{Al}_{1-x}\text{As}$  alloy whose lattice constants match. The problem is that of the mismatch between this pair of ternary alloys and their GaAs substrate. We first proposed that by the use of appropriate compositionally graded or superlattice buffer layers between the MQW's and the substrate we would be able to confine the misfit dislocations to the substrate/buffer interface - or at least to the buffer itself so that the MQW's would look at an essentially strain free interface. An attempt to explore the potential advantage of a heterojunction buffer layer was made by growing, by means of MBE, a  $0.5\text{ }\mu\text{m}$  thick nominally  $\text{In}_{0.3}\text{Al}_{0.7}\text{As}$  layer on a (100) - oriented GaAs substrate upon which were deposited sequentially ten QW's of  $\text{In}_{0.3}\text{Ga}_{0.7}\text{As}/\text{In}_{0.3}\text{Al}_{0.7}\text{As}$  (each of  $\sim 100\text{ }\text{\AA}$  thick, based on an assumed growth rate of  $130\text{ }\text{\AA}/\text{min}$  itself based on earlier calibration). Note that these compositions were well in excess of the theoretical limits for pseudomorphic growth. Transmission electron microscopic observation of the MQW's as well as of the buffer/substrate interface were encouraging although far from ideal. Relatively little buckling was observed in the quantum wells compared to earlier attempts using  $\text{In}_{0.25}\text{Ga}_{0.75}\text{As}/\text{GaAs}$  MQW's discussed in the last annual report. For most of the  $10\text{ }\mu\text{m}$  regions examined the quantum wells were flat from the buffer to the cap layer. There were a large number of micro twins originating primarily at the buffer/substrate interface extending through the MQW's to the surface. A few instances of

bulging of intermediate layers were found as well as some dislocation loops. The density of the dislocations appear to decrease from the buffer/substrate interface towards and through the MQW's. This result encouraged us to try a second experiment using essentially the same flux ratios except for a 1  $\mu\text{m}$  thick  $\text{In}_{0.3}\text{Al}_{0.7}\text{As}$  buffer layer. The transmission electron micrographs indicated a substantial reduction in the density of defects present in the MQW's; however, dislocation loops were still present, and some dislocations propagated through the MQW's. It becomes clear that increasing the thickness of the buffer layer is not going to solve, by itself, the problem of reducing the density of propagating defects or confining them within the buffer layer. On the other hand, we were also encouraged by the recent reports that the strained quantum wells themselves or a thin section of strained superlattice near the substrate may be used to take up the mismatch of the lattice constants by generating sufficient number of misfit dislocations in the superlattice near the substrate interface, without propagating the dislocations through the MQW's. Thus samples MBE-473, MBE-474, MBE-476 and MBE-514 were grown. MBE-473 consists of 80 periods of 100  $\text{\AA}$  thick  $\text{In}_{0.15}\text{Ga}_{0.85}\text{As}$  QW's with 100  $\text{\AA}$  thick GaAs barriers grown on GaAs, MBE-474 consists of 80 periods of 100  $\text{\AA}$   $\text{In}_{0.19}\text{Ga}_{0.81}\text{As}$  QW's with 100  $\text{\AA}$  GaAs barriers grown on GaAs, MBE-476 consists of 125 periods of 20  $\text{\AA}$   $\text{In}_{0.15}\text{Ga}_{0.85}\text{As}$ /20  $\text{\AA}$  GaAs superlattice on 1000  $\text{\AA}$  GaAs buffer, followed by 50 periods of 100  $\text{\AA}$   $\text{In}_{0.15}\text{Ga}_{0.85}\text{As}$ /100  $\text{\AA}$  GaAs MQW, then followed by 5 periods of superlattice cap while MBE-514 consists of 125 periods of 20  $\text{\AA}$   $\text{In}_{0.22}\text{Ga}_{0.78}\text{As}$ /20  $\text{\AA}$  GaAs superlattice grown on 1000  $\text{\AA}$  GaAs buffer, followed by 50 periods of 100  $\text{\AA}$   $\text{In}_{0.22}\text{Ga}_{0.76}\text{As}$ /100  $\text{\AA}$  GaAs MQW then followed by 5 periods of  $n^+$  superlattice cap. Figure 4(a), 4(b), 4(c) and 4(d) illustrates the material structure of MBE-473, MBE-474, MBE-476 and MBE-514. Figure 5(a), 5(b), 5(c) and 5(d) show the corresponding transmission spectra (after substrate absorption and reflection losses have been deducted) and electro-absorption spectra of the same samples. It is clear from these results that we have succeeded in obtaining many periods of good quality QW's. The percentage of absorption per well in sample MBE-476 is as good as that of the 10 MQW structure grown earlier. The narrowest photo-luminescence linewidth is obtained from sample MBE-476, which

has a thin superlattice buffer layer to take up the mismatch between the substrate and the MQW layers. Samples MBE-473 and MBE-474 are similar to those grown at MIT Lincoln Lab. The QW layers are grown directly on GaAs without buffer. The primary difference between them is the higher In concentration in MBE-474. TEM photographs made at Lockheed Research Laboratories show that, in MBE-473, there are dislocations in the GaAs near the QW/substrate interface, while in MBE-474 dislocations are seen throughout the quantum well layers, but not in the substrate. If a superlattice buffer is used such as in MBE-476, then dislocations are confined in the first few periods of the superlattice near the GaAs interface. If we compare the two structures with the same indium content, MBE-473 and MBE-476, the structure with the superlattice buffer has a larger peak absorption, narrower line width and larger electro-absorption than the one with no buffer. We believe that it is preferable to have dislocations occur in layers which are not optically active. If we compare the samples with different In concentration which are grown in the same manner (with or without superlattice buffer) then the one with smaller In content has larger peak absorption, narrower linewidth and larger electro-absorption. In general, better electro-absorption properties are obtained with a lower indium content and consequently smaller strain and by using a superlattice buffer layer.

## 5. ELECTRO-ABSORPTION MODULATION AT THE $1.06 \mu\text{m}$ WAVELENGTH

Notice that the wavelength for exciton absorption in MBE-474 has shifted toward longer wavelengths as the In content is increased, but not as far as one might expect if the strain were absent. It would be very desirable to have the peak of electro-absorption centered around the  $1.06 \mu\text{m}$  wavelength in order to take advantage of the availability of the high power Nd/YAG laser source. Thus MBE-569 was grown. Its structure is illustrated in Figure 6. It contained 3 QW's with  $\text{In}_{0.25}\text{Ga}_{0.75}\text{As}$  among MQW and superlattice structures with 19% In. In this case these quantum wells are pseudomorphic with the stack of quantum wells with 19% indium; they are sufficiently thin not to exceed the critical thickness. The stack of quantum wells are pseudomorphic to themselves, but not to the substrate. The superlattice is the buffer. Figure 7

shows its electro-absorption spectra. Clearly we have demonstrated a material structure that will provide modulation at the  $1.06\ \mu\text{m}$  wavelength. However, since there is no immediate requirement for SLM's at the  $1.06\ \mu\text{m}$  wavelength, further investigation of SLM's with reasonably large depth of modulation and low switching voltage has not been pursued.

## 6. AUTOMATION OF THE MBE GROWTH BY MEANS OF COMPUTER CONTROL

In order to increase the total number of QW layers and to obtain superlattice structures we embarked on the design and construction of a computerized controller. It is relatively inexpensive, has now been completed and tested. A paper, "Automatic Shutter Control for Molecular Beam Epitaxial Reactors", has been published in Review of Scientific Instruments, vol 59, p. 1246 (1988).

It consists of a microcomputer, (in our case an Apple Macintosh) connected to a programmable scanner (in our case a Keithley Model 705 which has an IEEE 488 compatible interface). The scanner allows the selection of any one or any combination of eight single pole switches that operate the eight available effusion cell furnace shutters of the MBE reactor. The microcomputer is programmed to select the primary address, dwell time, control intervals of the switch combinations required to operate the MBE. In view of the fact the Macintosh has a serial RS-232C output an I/O interface has had to be introduced to make it compatible with the IEEE-488 input to the scanner (in our case a Mac 488A bus controller made by I/O Tech). The scanner output is connected to an electronic solid state relay system designed and built at UCSD in accordance with AIE Standard RS-422-A specification. Each solid state relay acts as a shunt switch across the manual switches provided by the console of the MBE reactor which operates the pneumatic shutters. The relay controller can thus be operated either in the manual or computer-controlled mode with appropriate time delays introduced as needed to achieve near steady-state epitaxial growth.

Initial results obtained with this system were highly satisfactory. Successful growth of the samples MBE-473, MBE-474 and MBE-476 are the best evidence that the automated system is

functioning properly.

## 7. DESIGN OF SLM TO OBTAIN LARGE MODULATION DEPTH - THE REFLECTION MODE

It is clear from the data presented in Figure 5 that change of total transmittance (or absorption) in the range of 30% to 40% can be obtained from 50 to 80 MQW of  $\text{In}_x\text{Ga}_{1-x}\text{As}/\text{GaAs}$ . This is not enough for many SLM applications. Larger number of wells will increase the modulation depth. However, even using a buffer layer, there may be a limit on the number of wells that can be grown without creating eventually massive dislocations. Increase of the number of wells will also call for an increase of applied voltage to yield the same electric field. Large switching voltage is also undesirable. A reflection mode modulator could double the absorption without the penalty of increased switching voltage. Therefore material structures to provide reflections have been investigated in two ways: (a) The growth of AlAs layers,  $\lambda/4$  thick, interwoven with GaAs layers,  $\lambda/4$  thick, to form a dielectric grating mirror. (b) The use of metal film deposited on top of the semiconductor as a reflector.

Early experiment of reflection mode EA used a p-doped GaAs substrate and the Cr/Au electrode of the p-i-n diode as the reflector. It failed. There is too much attenuation due to the p-doping. In addition there is a problem with the reflectivity of the Cr/Au layer on the GaAs cap layer. A control experiment was performed to measure the reflectivity from (a) a GaAs/air interface, (b) a GaAs coated with Cr/Au (c) a GaAs coated with a  $\lambda/4$  thick layer of  $\text{SiN}_x$ , then coated with Cr/Au. The measured reflectivities are (a) 33%, (b) 50% and (c) 65%. This confirmed our earlier preliminary conclusion that there may be interdiffusion or other reaction between Cr/Au and GaAs, reducing substantially the reflectivity of the metal. Further experiments will be carried out to obtain the maximum reflection that can be obtained from  $\text{SiN}_x$  and Cr/Au coatings. Such a reflector is important for SLM applications that require the optical beam to be incident on the substrate. We have also grown alternative layers of AlAs,  $\lambda/4$ , interwoven with GaAs layers,  $\lambda/4$  thick, to form a dielectric Bragg grating reflector. Figure 8

shows the reflection spectra of this sample. A maximum reflectivity of 95% has been obtained. Further experiments to characterize MQW modulator structures grown on top of this reflector is underway at UCSD, including the effects of interference reflections from this mirror and the GaAs/air interference. Such a reflection modulator would require the optical beam to incident on the sample from the cap layer side as it may be difficult to grow a thick mirror on top of the MQW layers that are already under strain.

## **8. DESIGN OF SLM TO OBTAIN LARGE MODULATION DEPTH - BUFFER AND SUBSTRATE ABSORPTION**

If there is significant absorption from the substrate or the buffer layer, there will also be a reduction of the SLM modulation depth. Since we have developed recently the technology of p-doping of epitaxial layers, we are now using SI substrate with a thin p-doped GaAs layer grown epitaxially on top for the p-contact of the p-i-n modulator. We had assumed, so far, that the semi-insulating GaAs substrate and the buffer should be transparent at photon energies significantly lower than the GaAs bandgap energy. However, when we grew MBE572 for the investigation of the non-linear effect in another research project, we were surprised that there is a residue absorption in that SI substrate that cannot be saturated. This triggered us to investigate the absorption of the GaAs substrate and the superlattice buffer (used to relieve the strain of the quantum well layers as discussed in section 4). Figure 9 shows the structural schematic diagram of MBE 572. It is similar to the other samples that we have grown for this project. It has a SI GaAs substrate 840  $\mu\text{m}$  thick and a superlattice buffer layer 2000  $\text{\AA}$  thick. The residual absorption must come from either the substrate or the superlattice buffer.

The substrate for MBE 572 (without any layer grown by MBE) was examined by a calibrated Cary 2400 spectrophotometer at the Naval Ocean System Center. It showed a residual material absorbance of 0.263 A at 0.99  $\mu\text{m}$  wavelength, after all the reflection losses have been deducted. Absorbance A is defined as  $\log_{10}$  (input power/output power). This absorbance was confirmed by another independent measurement where a Nd/YAG laser beam at 1.06  $\mu\text{m}$  is



transmitted through the substrate at the Brewster angle. On the other hand, when another SI substrate, #349S50, was examined by the same procedure, it showed only a material absorption of 0.008 A. Thus we concluded that the selection of the substrate material is important to assure us low material absorption in the substrate in the future.

The situation with superlattice buffer is quite different. Figure 10 show the transmission of samples MBE 661, MBE 662, and MBE 663 as a function of wavelength. Clearly the superlattices have their own absorption edge which varies with indium concentration. Figure 11 shows the structural schematic diagram of MBE 662. Samples MBE 661 and MBE 663 are identical with MBE 662 except the indium concentrations are 12% and 19%, respectively. These superlattice layers are very similar to the superlattice layer we have used in samples MBE 476 and MBE 514 shown in Figures 4 and 5. We conclude that the absorption edge of superlattice may interfere with the operation of the modulator depending on the photon energy. Notice the absorption coefficient is very large as the total thickness of superlattice is only 1.2  $\mu\text{m}$ . Subsequent experiments show that superlattices similar to these samples exhibit also Franz-Keldysh like EA effect. This made the superlattice itself very interesting as a material for modulators. The use of superlattice and coupled quantum well structures for modulation is currently being pursued in other research projects at UCSD. As for the design of MQW spatial light modulators, we have two choices. (1) We will base our design on structures similar to MBE 473, using 15% indium in the quantum wells. In this case we depend on the generation and the confinement of dislocations in the first few quantum wells near the substrate interface to relieve the strain. (2) We will continue to use superlattice as the buffer. Further investigation will be conducted to make sure that the superlattice period and composition will not cause significant attenuation at the operating wavelength of the SLM.

## 9. DEMONSTRATION OF THE OPTICAL-OPTICAL INTERACTION IN A MQW DETECTOR-MODULATOR DIODE PAIR

As a first step toward the realization of a MQW spatial light modulator array, we have fabricated two diodes on a SL MQW sample (MBE-322) which contains 10 periods of  $85 \text{ \AA} \text{ In}_{0.12}\text{Ga}_{0.88}\text{As}/100 \text{ \AA} \text{ GaAs}$  with  $3000 \text{ \AA}$  of SI GaAs buffer and n-GaAs cap layers. This constitutes a single cell in an array. The diode top electrode consists of a Cr/Au  $3.4 \text{ mm} \times 3.4 \text{ mm}$  square with a  $2 \text{ mm}$  window to pass through the light. The two diodes were externally connected in parallel and biased to  $V_R = 2.4 \text{ volt}$  through a load resistor  $R_L = 5.1 \text{ K } \Omega$ . The diode on one side is used as a detector for He-Ne laser radiation at  $\lambda = 0.6328 \mu\text{m}$ . The diode on the other side is used as the modulator for the radiation generated by a tunable pulsed dye laser-parametric oscillator.

Since then we have also developed the technique for p-doping in our MBE system. Figure 13 illustrates the monolithically integrated modulation/detector diode pair that has recently been fabricated based on sample MBE-533. MBE-533 consists of 50 periods undoped ( $20 \text{ \AA}$ )  $\text{In}_{0.15}\text{Ga}_{0.85}\text{As}/(20 \text{ \AA})\text{GaAs}$  superlattice buffer on p-GaAs substrate, followed by 50 periods of ( $70 \text{ \AA}$ )  $\text{In}_{0.15}\text{Ga}_{0.85}\text{As}/(100 \text{ \AA})\text{GaAs}$  QW's, 20 periods of undoped ( $20 \text{ \AA}$ )  $\text{In}_{0.15}\text{Ga}_{0.85}\text{As}/(20 \text{ \AA})\text{GaAs}$  superlattice buffer,  $2000 \text{ \AA}$  of n-doped GaAs and  $1000 \text{ \AA}$  of p-doped GaAs. Zn/Au and Cr/Au electrode contacts are fabricated by photolithography on p-GaAs and n-GaAs respectively. A technique for plating of gold on the Zn/Au and Cr/Au electrodes was developed so that gold wires can be bonded to the contact without damaging the QW structure below. The thick plated gold protected the QW's below. Each electrode has only a  $100 \mu\text{m}$  diameter hole for transmission of light. The small electrode pattern is used both to reduce the leakage current under reverse bias and to reduce the device capacitance to increase the frequency response. The diodes were connected in parallel to the d.c. power supply ( $V_c = 5 \text{ volts}$ ) as shown in Figure 13. The p-n GaAs diode is the detector while the n-i-p diode serves as the modulator. The leakage current is less than  $5 \mu\text{A}$ . As a He-Ne laser light illuminates the detector diode,  $V_\alpha$  is dropped from  $4.8$  to  $0.7 \text{ V}$  creating a  $15.5\%$  increase of the transmitted

light at the 9655 Å wavelength from the pulsed dye laser/parametric oscillator. Figure 14 shows the electro-absorption data of the modulator at various wavelength for  $V_d = 0$  and  $V_d = 5$  volts. He-Ne laser and pulsed dye laser/parametric oscillator are used because of the delays in the delivery of the CW tunable dye laser and the Ti-sapphire laser to be pumped by an argon laser. In summary, we have solved successfully some of the fabrication problems of integrating monolithically photo diodes with MQW samples and have demonstrated that optical-optical interaction in a MQW detector/modulator pair is feasible.

## 10. CONCLUSION AND FUTURE WORK

During this contract period, we started from the initial concepts of strained quantum wells and  $\text{In}_x\text{Ga}_{1-x}\text{As}$  quantum well material on GaAs as potential effective material structure for SLM applications. We have explored many materials and device issues of this complex material/device system. We have successfully demonstrated sharp EA spectra in this material system and overcame the conventional limitation on the number of SL quantum wells that can be grown. Over 30% modulation of the transmitted light has been observed, when substrate attenuation is excluded. We have also demonstrated in a preliminary fashion the feasibility of optically addressed SLM using a detector/modulator monolithically integrated on the same chip.

Since 1987, we have entered into the second phase, namely modulator design optimization. So far, we have established a fundamental understanding of the relationship among quantum well depth, quantum well thickness, the shift of the exciton peak and the change of the magnitude of exciton absorption strength. This knowledge is important to both the choice of negative and positive EA mechanisms for a given application and the design of quantum wells for maximizing the modulation effect with minimum required voltage across each period of the QW. We have shown the advantages of using the reflection mode and the issues on reflectors that must be resolved in order to realize the potential of this method. We have identified and characterized the possible mechanisms of substrate and buffer layer absorption that will be avoided in future devices. In the one-year continuing grant, AFOSR contract No. 89-0254, we

intend to take into account all of these considerations in order to obtain a p-i-n reflection modulator with reasonably large modulation depth (e.g. larger than 50%) and low operating voltage (e.g. 5 volts). In addition we are fabricating a 2 dimensional array of p-i-n modulators for Prof. Sadik Esener to use either electron beam or microchannel plate to address.

A number of issues remain to be unresolved. These issues are very important to the successful operation of such a modulator array. They include:

- (1) The capacitance of the p-i-n modulator diode.
- (2) The linearity of the modulator, and, if necessary, methods to improve the linearity.
- (3) The extinction ratio and the linear dynamic range.
- (4) The insertion loss and the potential of using positive EA for reduction of insertion loss.
- (5) The effect of the voltage drop on the p-i-n reverse biased diode created by the generation of carriers by the signal radiation. As an alternative, the use of ER for modulation would minimize the photo generated carriers.

These issues will be investigated during the one-year period of contract AFOSR 89-0254 as time permits.

TABLE 2.

The mechanisms by which the quantum well parameters affect the electroabsorption characteristics. The "+" sign indicates an enhancement of the EA effect, "-" sign indicates a reduction.

Cause	Effect	Positive	Negative
		EA	EA
Increase $L_z$	Smaller $f$	--	--
	$\Delta E/F^2$ larger	+	+++
	$\Delta I/F_{sup2}$ larger	--	+
	$\Delta I/\Delta E$ larger	--	+
	Larger forbidden level spacing		-
	Smaller interface roughness broadening	++	++
	Larger field nonuniformity	--	--
Decrease $\Delta E_c$ , $\Delta E_v$	Smaller $f$	--	--
	$\Delta E/F^2$ larger	+	+++
	$\Delta I/F^2$ larger	--	+
	$\Delta I/\Delta E$ larger	--	+
	Larger forbidden level spacing		-
	Smaller interface roughness broadening	++	++
Increase $E_g$	Larger $f$	++	++

## 11. PAPERS PRESENTED, PUBLISHED AND ACCEPTED

1. L. M. Walpita, W. S. C. Chang, H. H. Wieder and T. E. Van Eck, "Cross Modulation of Light in Semiconductor Materials in the Presence of Electric Fields" *Applied Optics*, **24**, 2481 (1985).
2. L. M. Walpita, W. S. C. Chang, H. H. Wieder and T. E. Van Eck, "Modulation of an Optical Beam by a Second Optical Beam in Biased Semi-insulating GaAs", *Picosecond Electronics and Optoelectronics*, edited by G. A. Morrow, D. M. Bloom and C. H. Lee, Springer Verlag, NY, 176 (1986).
3. T. E. Van Eck, P. Chu, W. S. C. Chang and H. H. Wieder, "Electro-Absorption in an InGaAs/GaAs Strained Layer Multiple Quantum Well Structure", *Appl. Phys. Lett.*, **49**, 135-136 (1986).
4. T. E. Van Eck, L. M. Walpita, W. S. C. Chang and H. H. Wieder, "Franz-Keldysh Electro-Refractive and Electro-Absorption in Bulk InP and GaAs", *Appl. Phys. Lett.* **48**, 451-453 (1986).
5. T. E. Van Eck, P. Chu, W. S. C. Chang and H. H. Wieder, "Electro-Optic Modulation in an InGaAs/GaAs Strained Layer Multiple Quantum Well Structure", Paper presented at the Optical Society of American Annual Meeting, Seattle, Washington (1986).
6. W. S. C. Chang, H. H. Wieder, T. E. Van Eck, A. L. Kellner and P. Chu "Electro-Optical Properties of III-V Compound Semiconductors for Spatial Light Modulation Applications", SPIE Advanced Institute of Hybrid and Optical Computers, Leesburg, VA, March (1986).
7. C. C. sun, W. S. C. Chang and H. H. Wieder, "The Gate Controlled Photo-diode for Optical Matrix Multiplication Applications", Paper presented in the SPIE International Symposium on Optical and Opto-Electronic Engineering, San Diego, CA August (1986).
8. T. E. Van Eck and W. S. C. Chang, "Electrorefraction and electroabsorption in InGaAs/GaAs multiple-quantum-well structures", Paper presented at the Conference on Lasers and Electro-Optics, April 16 - May 1, 1987, Baltimore, MD.

9. W. S. C. Chang "Research in Materials and Components for Opto-electronic Signal Processing and Computing" paper presented at the DARPA/DSO Review Meeting, February 1-13, 1987, Xerox Training Center, Leesburg, VA.
10. W. S. C. Chang and T. E. Van Eck "Optic Waveguides and Electro-optical Devices in Heterojunction and Quantum Well Structures of III-V Compound Semiconductors, A Review", Invited talk at the SPIE O-E/Fibers Symposium, Aug. 16-21, 1987, San Diego, CA.
11. C. L. Lin, P. Chu, A. L. Kellner and H. H. Wieder, "Composition dependence of  $\text{Au-In}_x\text{Al}_{1-x}\text{As}$  Schottky barrier heights", *Applied Physics Letters*, vol 49, 1593 (1986).
12. P. Chu, C. H. Lin, A. L. Kellner, W. S. C. Chang and H. H. Wieder, "Molecular Beam Synthesis and Properties of  $\text{In}_x\text{Al}_{1-x}\text{As}$  Strained Layers", Presented at International Conference on Superlattices and Microstructures, Chicago, August (1987).
13. H. H. Wieder, "Strained Layer Heterojunction Structures for High Frequency Applications" in DARPA Technical Document 1079 "EHF Monolithic Materials and Devices", May 1987.
14. S. Niki, Peter Chu, W. S. C. Chang and H. H. Wieder, " Automatic Shutter Control for Molecular Beam Epitaxial Reactors" *Review of Scientific Instruments*, 59, 1246 (1988).
15. T. E. Van Eck, S. Niki, P. Chu, W. S. C. Chang, H. H. Wieder and D. Coffey, "Design considerations for Multiple Quantum Well Modulators", Paper presented at the 1988 LEOS Annual Meeting, Santa Clara, Oct., 1988.
16. T. E. Van Eck, Ph.D. Thesis, "Electro-Optic Modulation in  $\text{InGaAs/GaAs}$  Strained Multiple Quantum Well Structures", 1988.
17. C. C. Sun, Ph.D. Thesis, "The Gate-Controlled Photodiode (GCPD) For Optical Signal Processing" 1988.
18. C. C. Sun, H. H. Wieder and W. S. C. Chang, "A New Semiconductor Device - The Gate - Controlled Photodiode: Device Concept and Experimental Results", To be published by

*IEEE J. of Quantum Electronics.*

19. S. Niki, C. L. Lin, W. S. C. Chang, and H. H. Wieder, "Band-edge discontinuities of strained layer  $\text{In}_x\text{Ga}_{1-x}\text{As}/\text{GaAs}$  heterojunctions and quantum wells". Presented for publication.



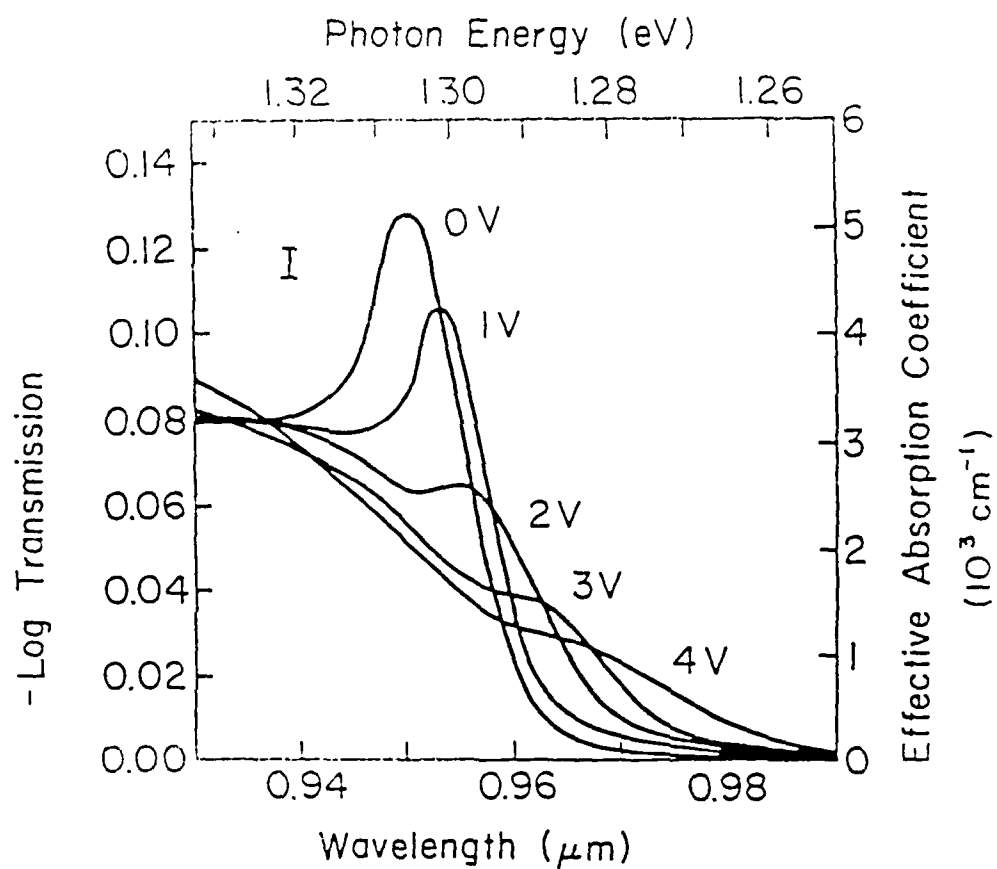


Figure 1. Electroabsorption spectra of MBE-110.

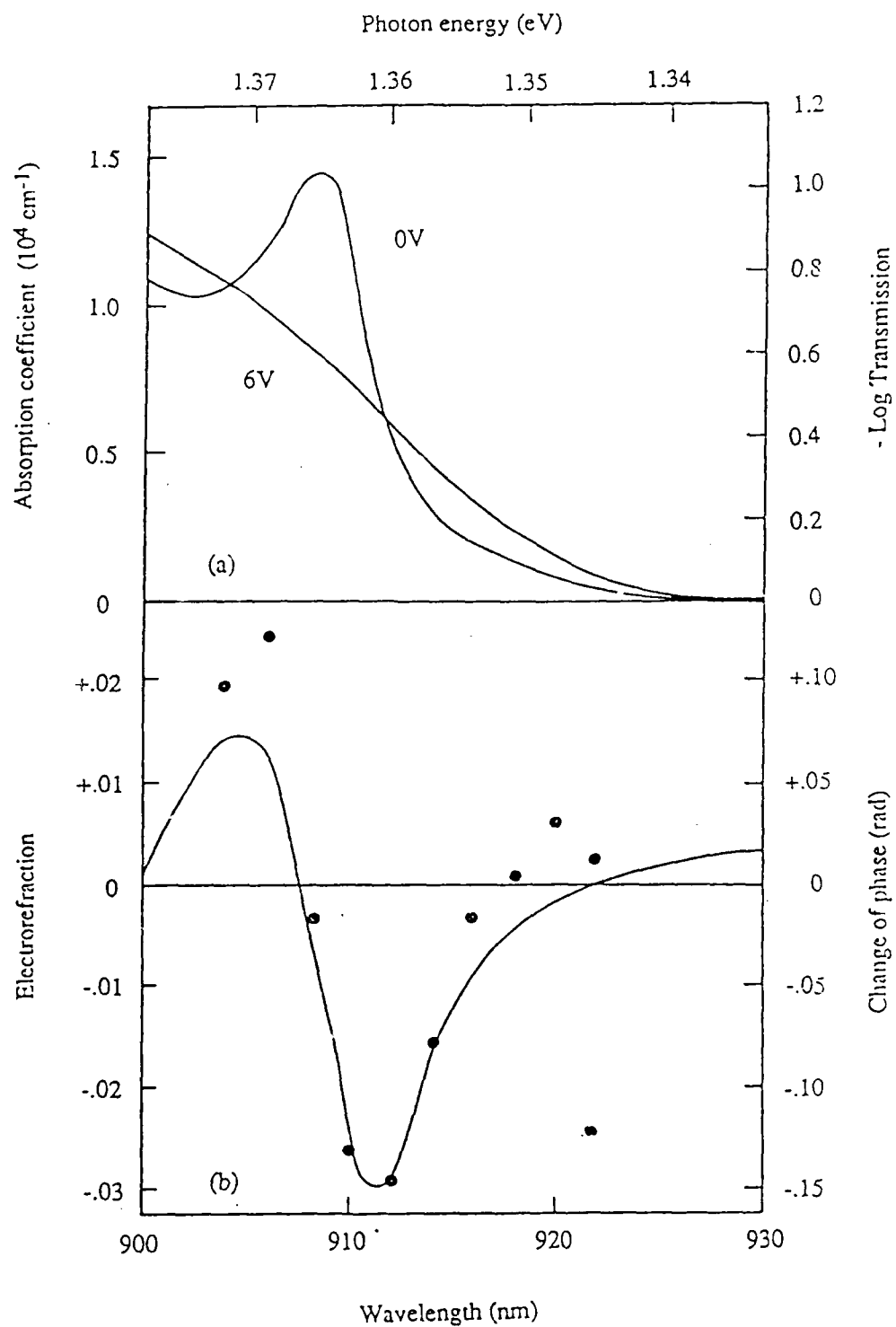


Figure 2. (a) Absorption spectra and (b) electrorefraction spectra of the 60 quantum well InGaAs/GaAs structure fabricated at MIT Lincoln Laboratory.

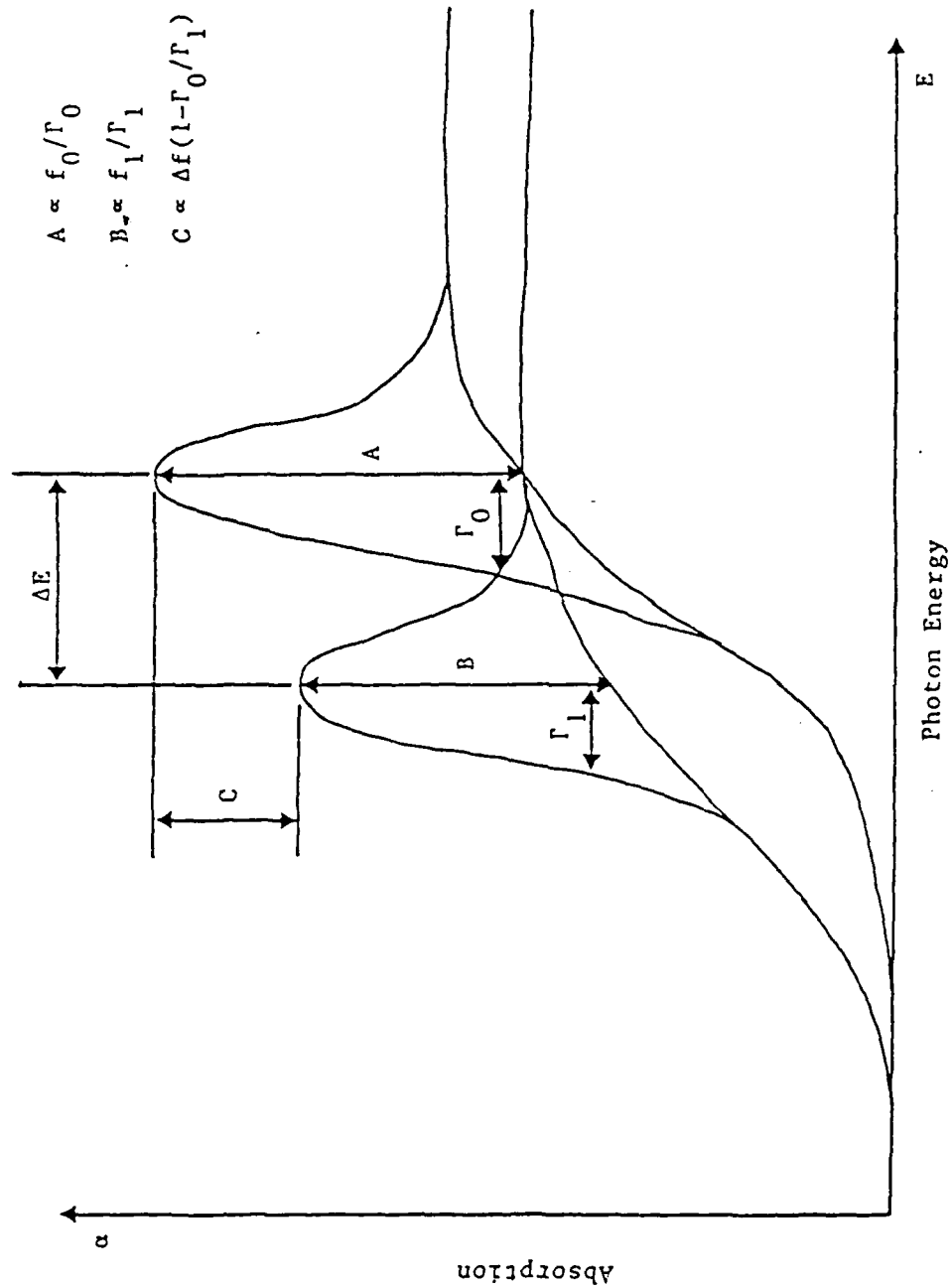


Fig. 3. Illustration of the parameters describing electro-absorption.

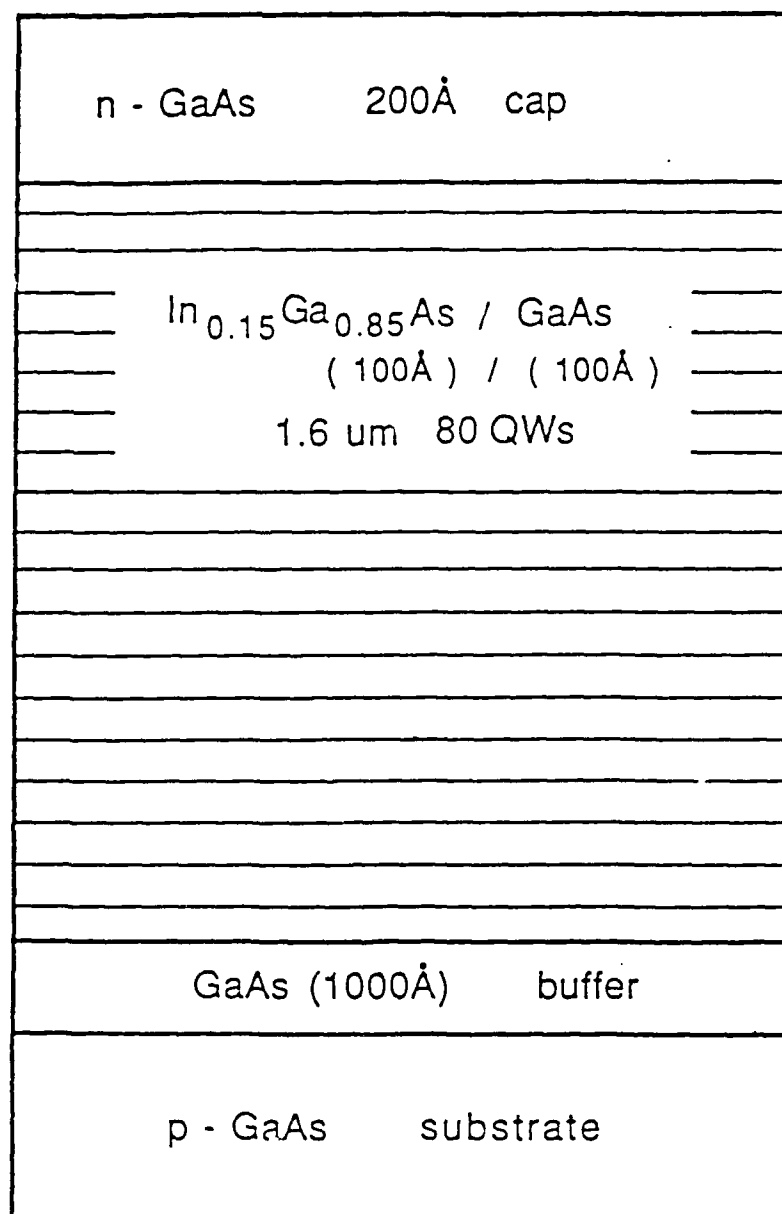


Fig. 4a. Schematic of the sample MBE 473

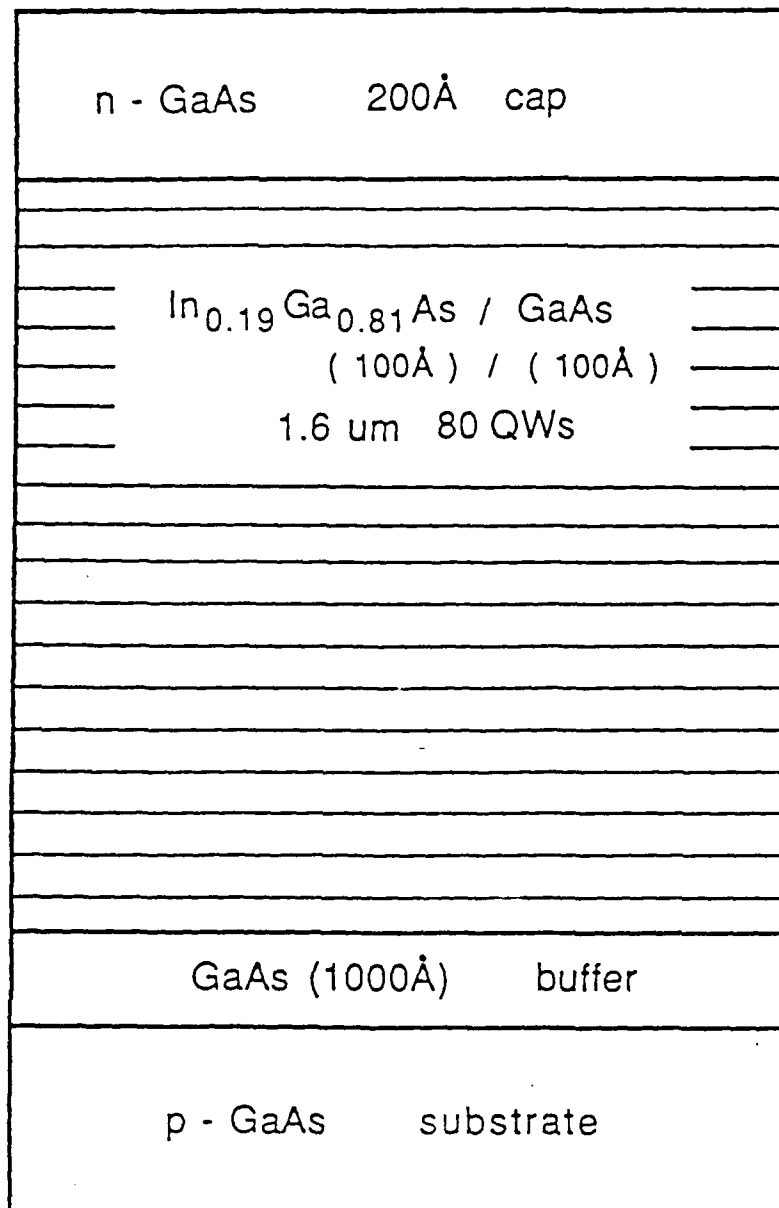


Fig. 4b. Schematic of the sample MBE 474

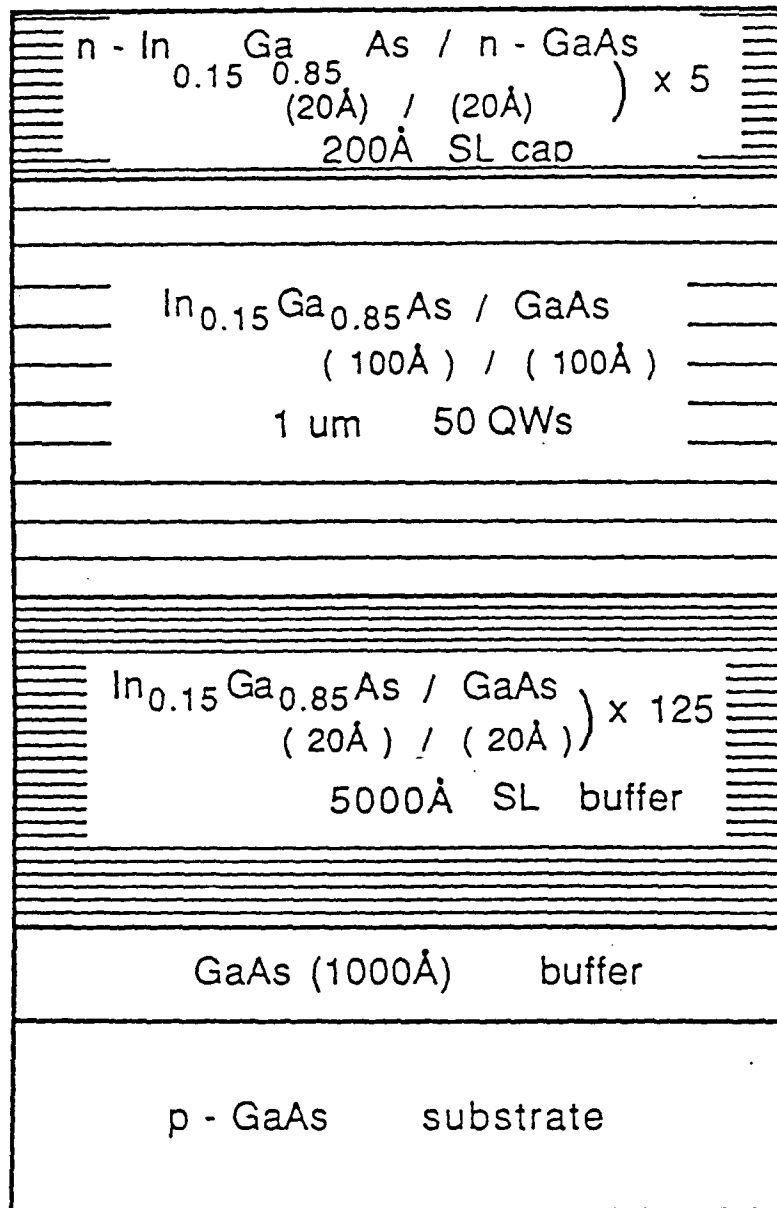


Fig. 4c. Schematic of the sample MBE 476

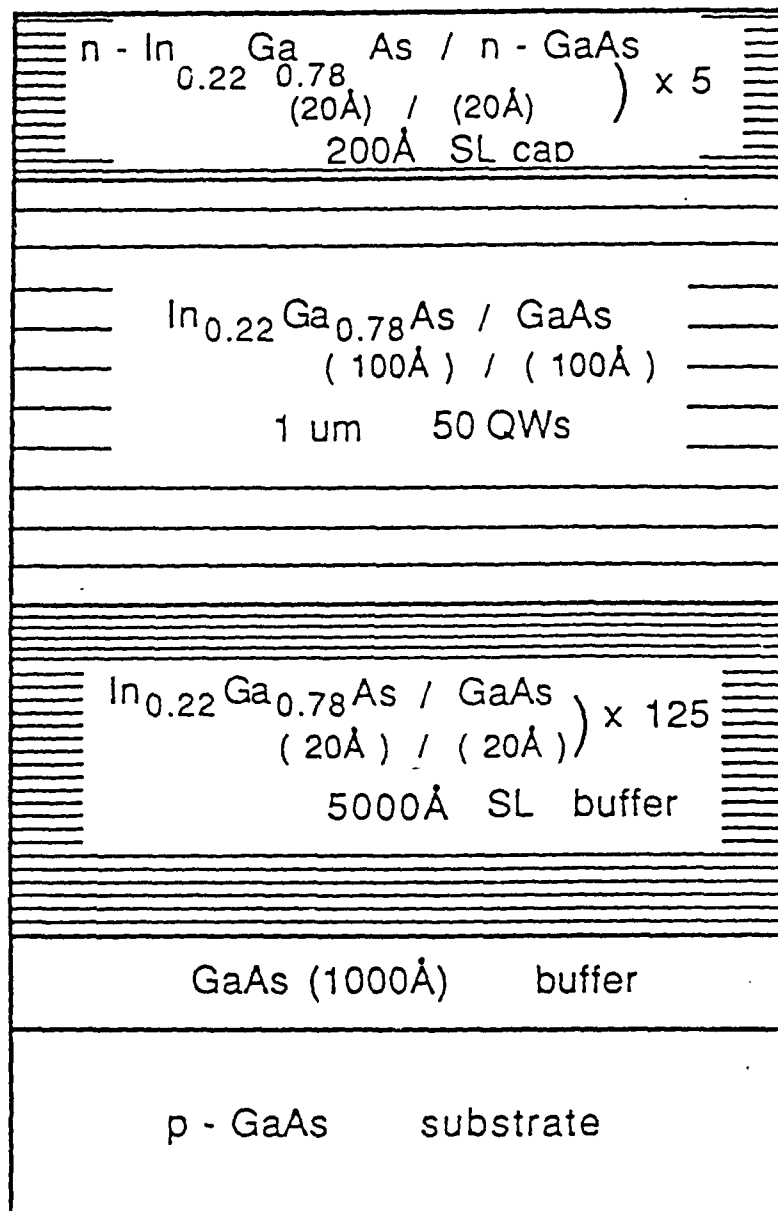


Fig. 4d. Schematic of the sample MBE 514

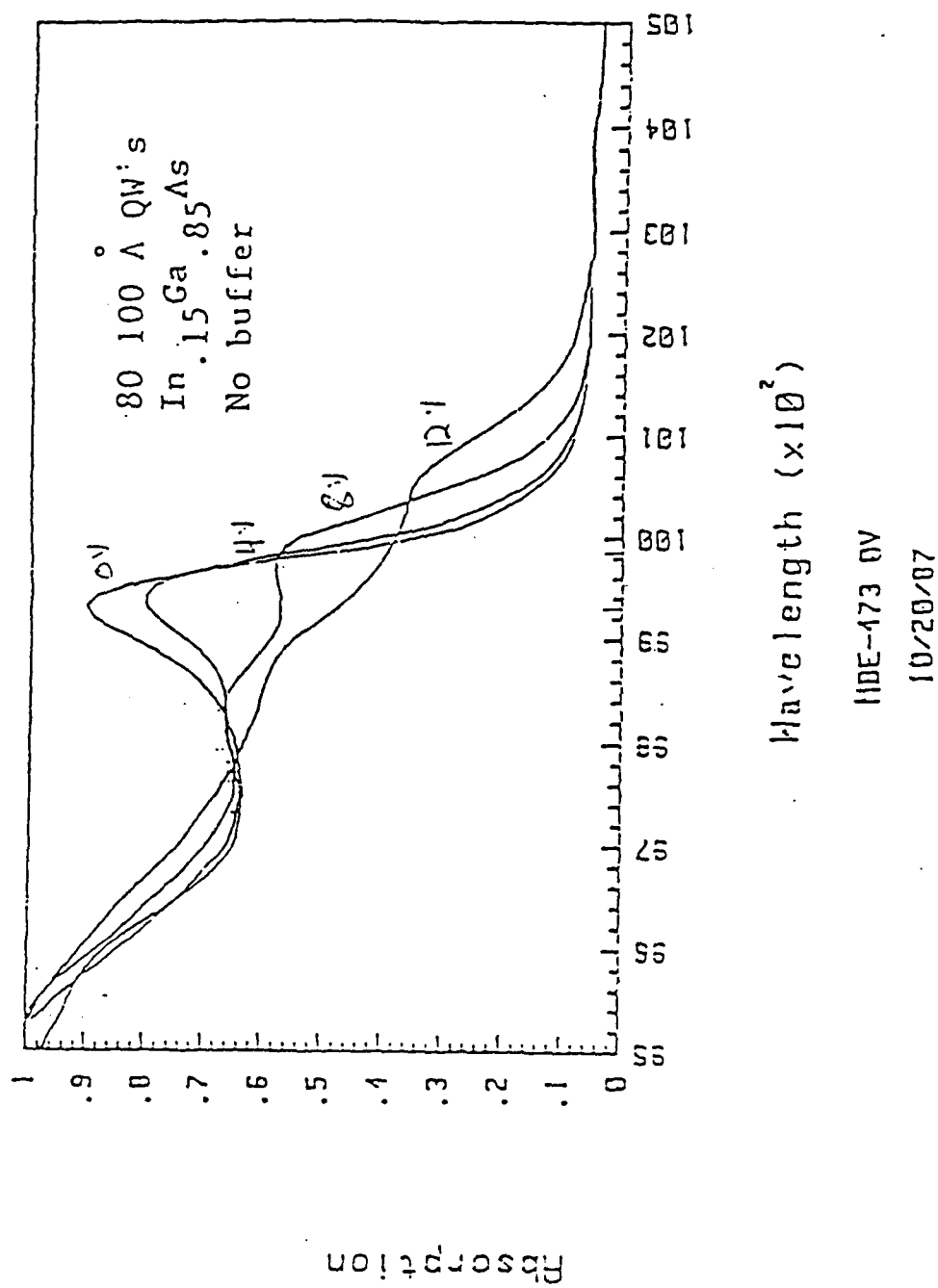


Fig. 5a. Absorption and electro-absorption spectra of sample MBE-473.



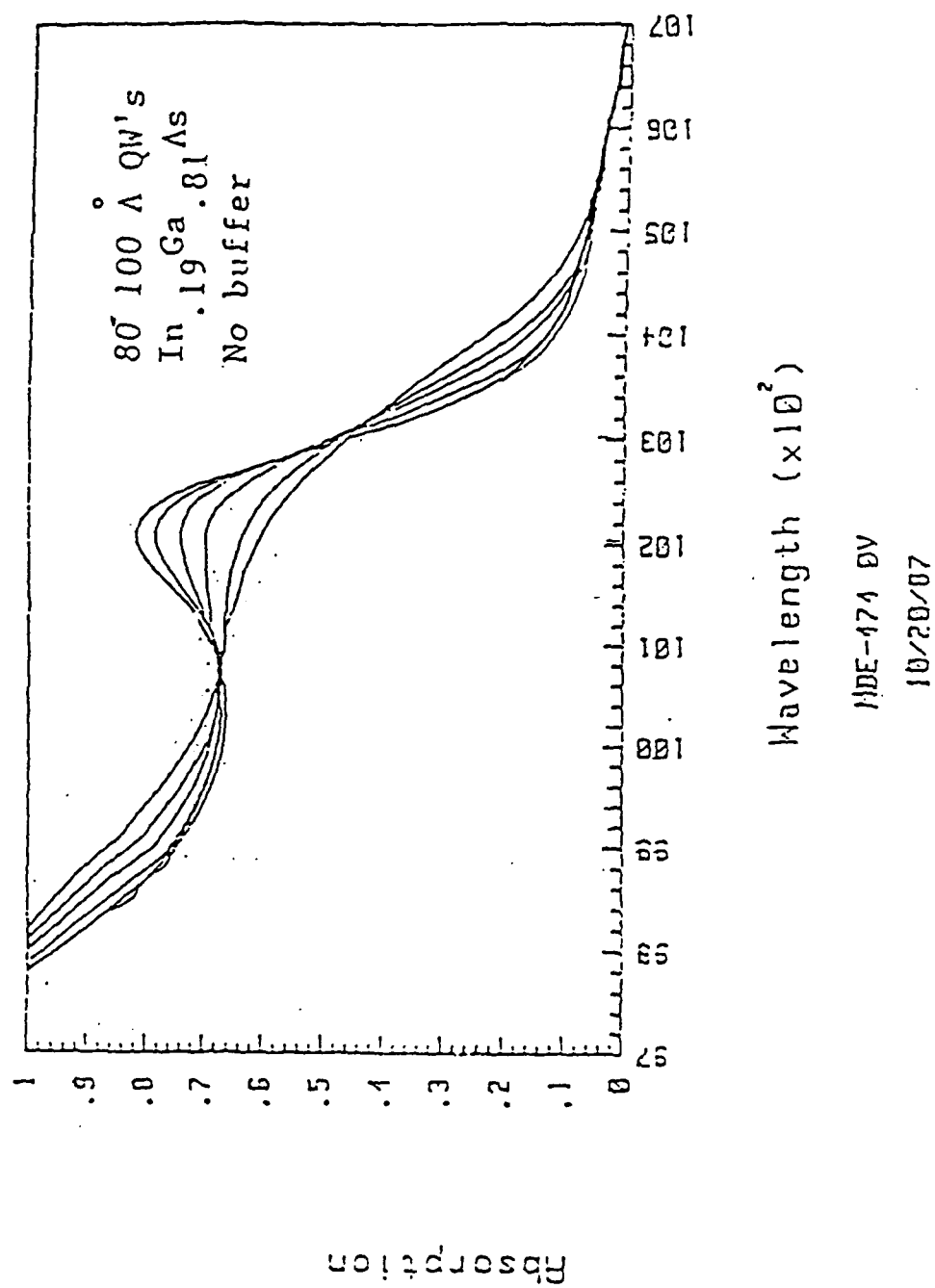


Fig. 5b. Absorption and electro-absorption spectra of sample MBE-474.

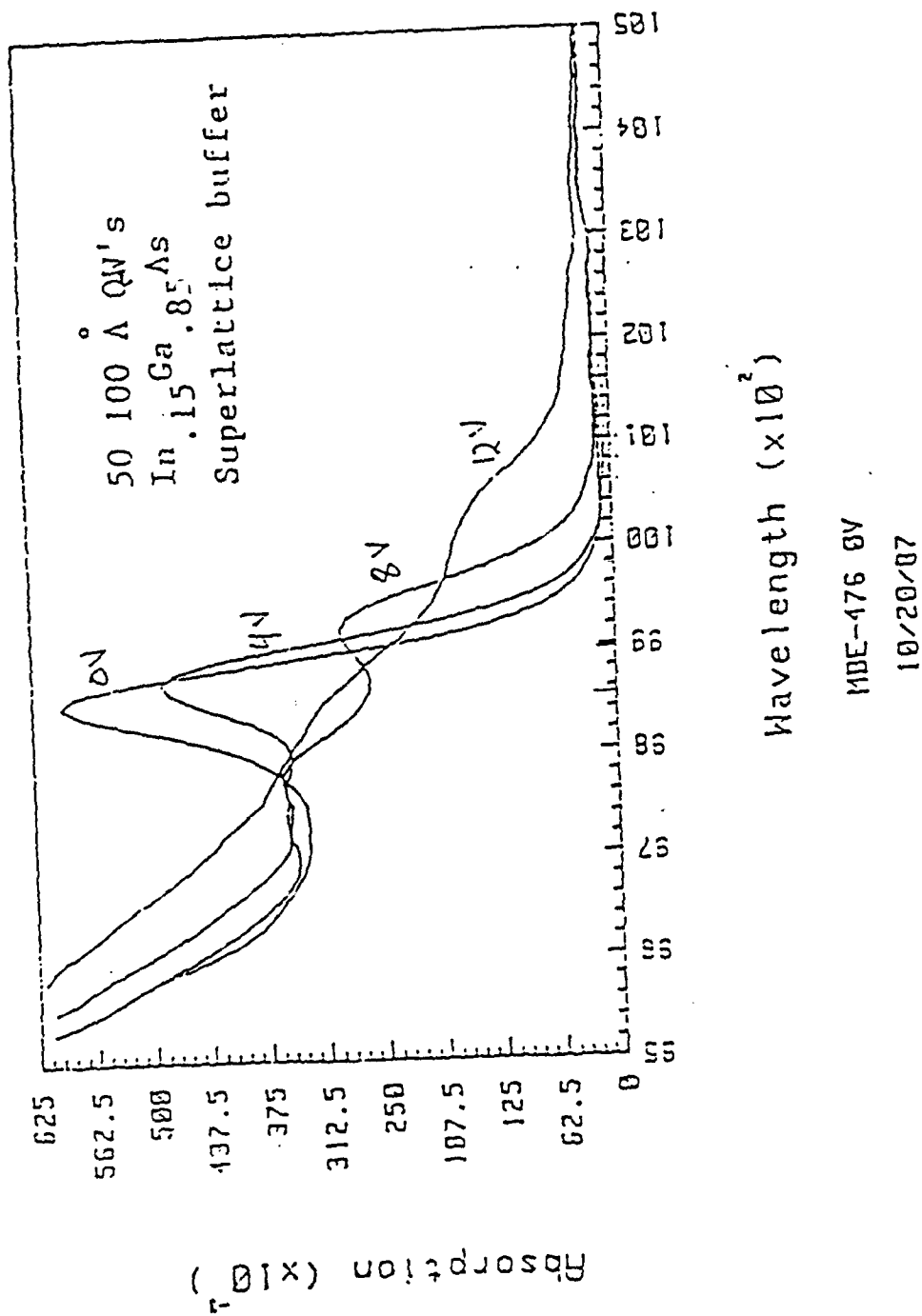
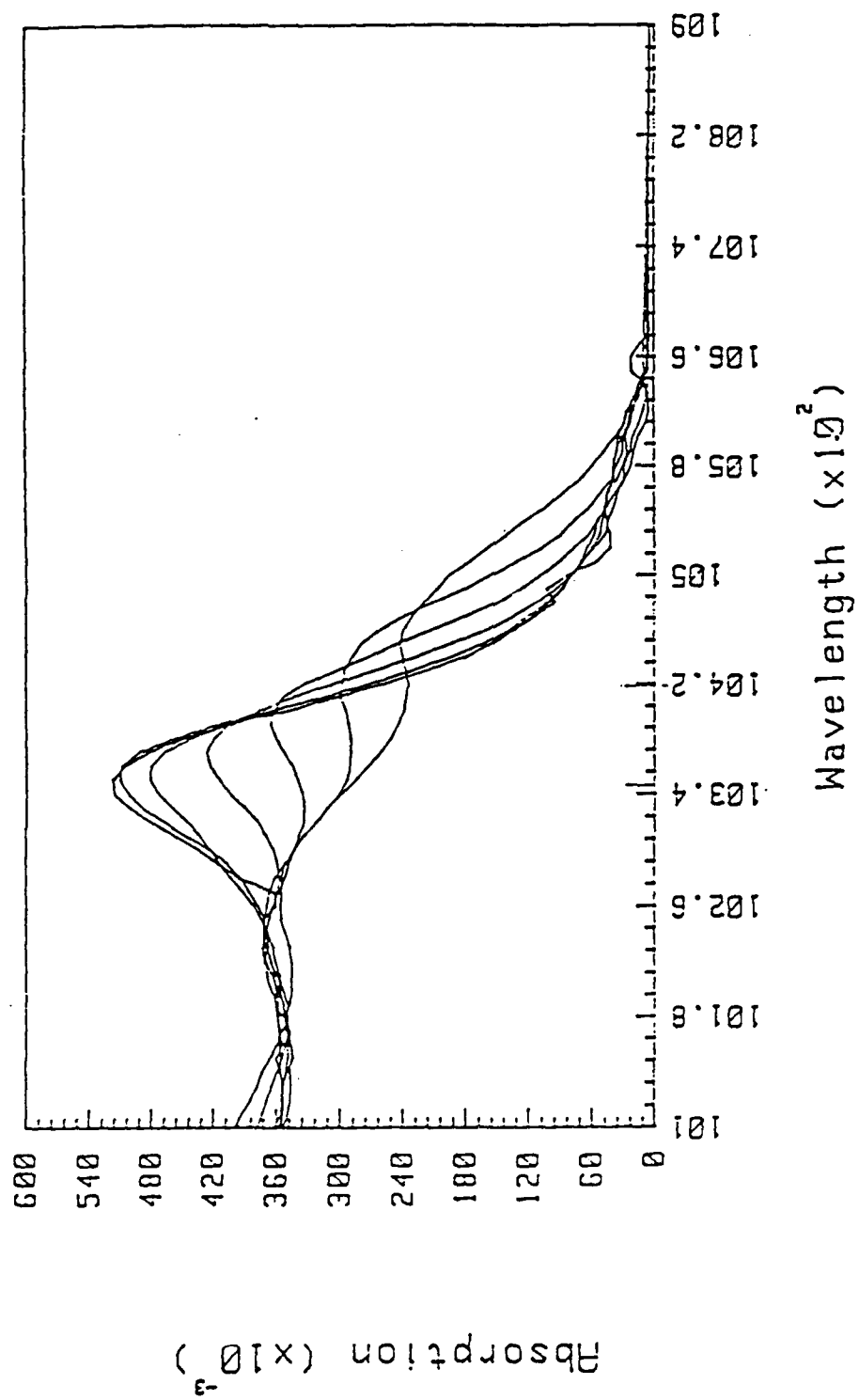


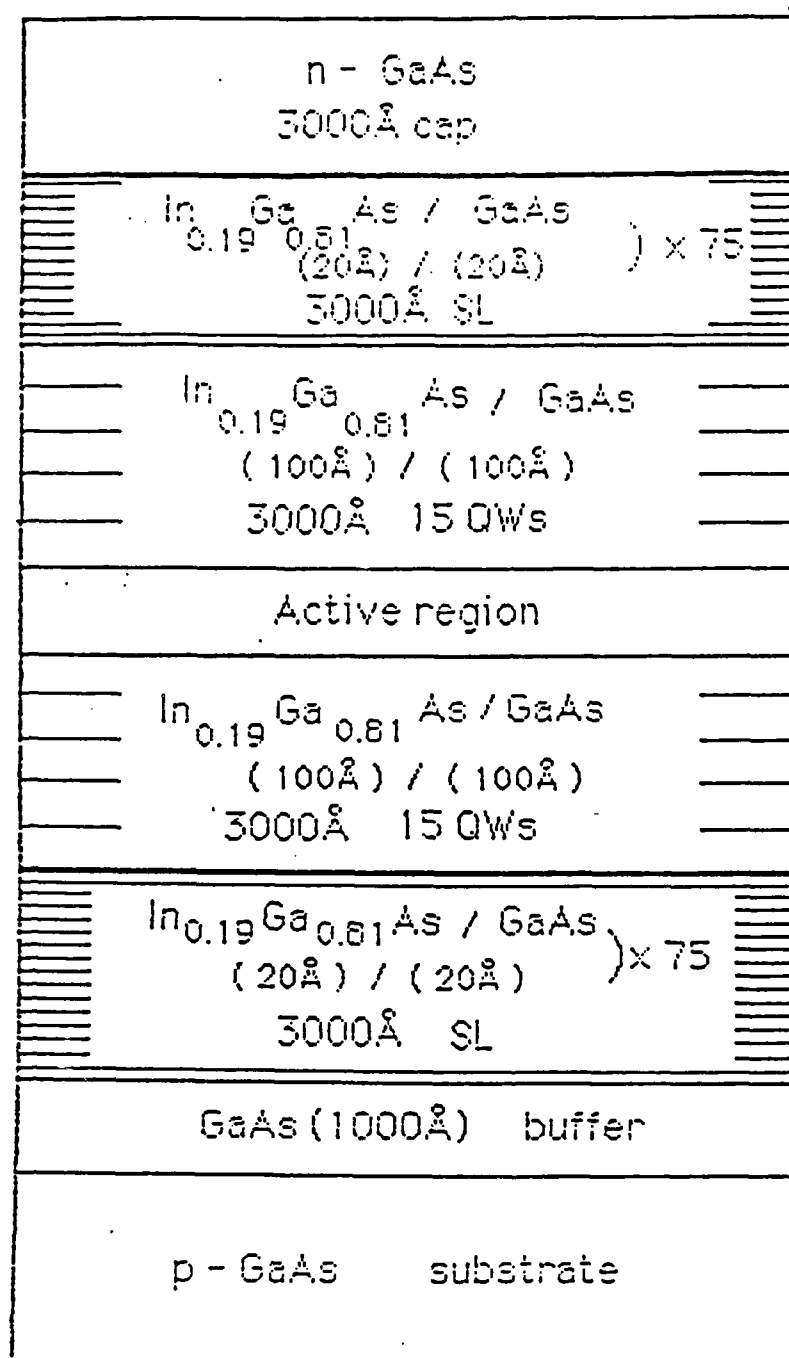
Fig. 5c. Absorption and electro-absorption spectra of sample MDE-476.



1/29/80 22% In 50 QW's

MBE-514-1g 0v

Fig. 5 d. Absorption and electro-absorption spectra of sample MBE-514.



$\text{In}_{0.25}\text{Ga}_{0.75}\text{As} / \text{GaAs}$   
 $(105\text{\AA}) / (100\text{\AA})$   
 615Å 3QWs

Fig. 6. Schematic of the sample MBE 569

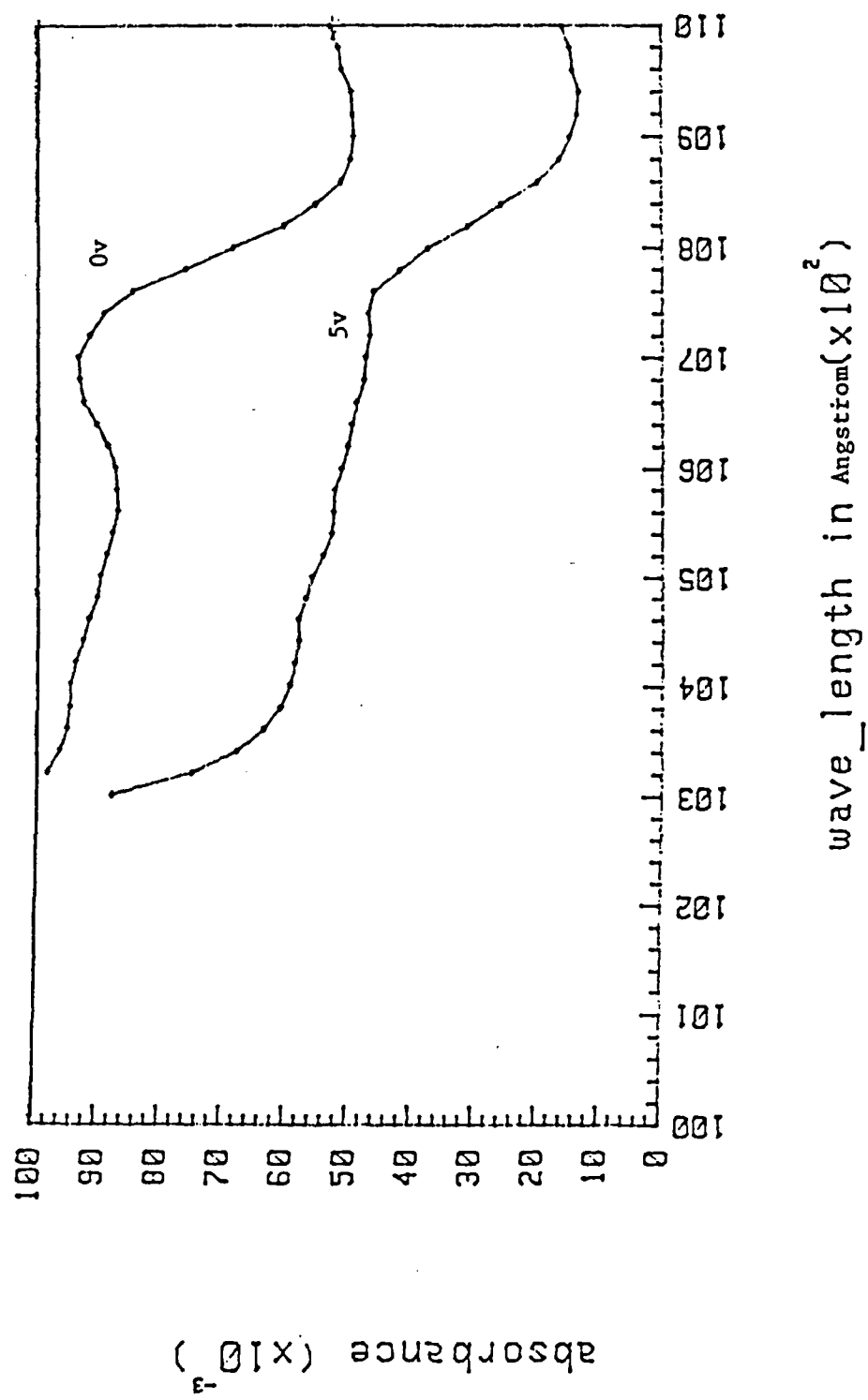


Figure 7. The Exciton Absorption Spectra at 0v and at 5v.

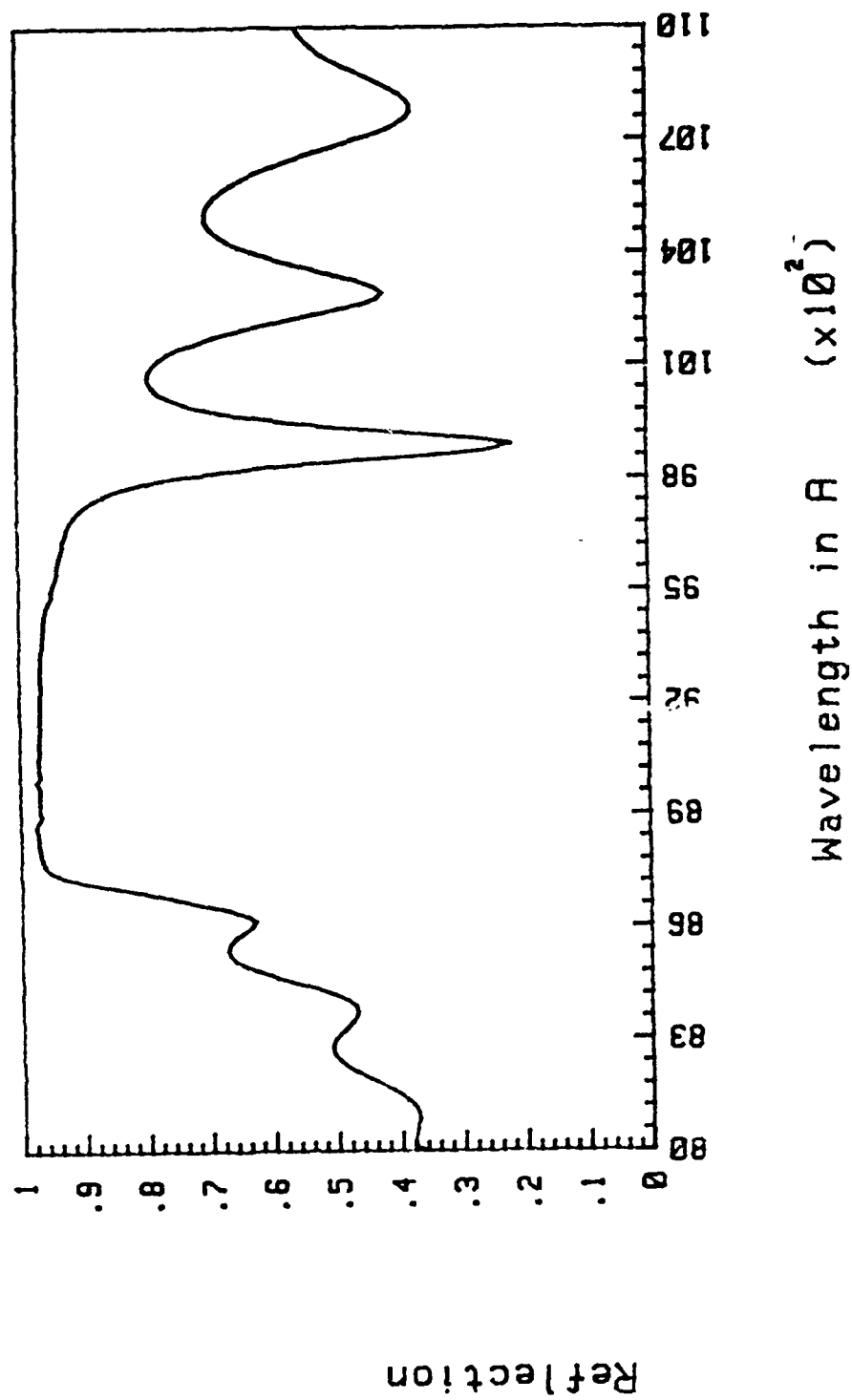


Fig. 8. Reflection Spectra of the AlAs/GaAs Bragg Reflection. Grating Mirror.

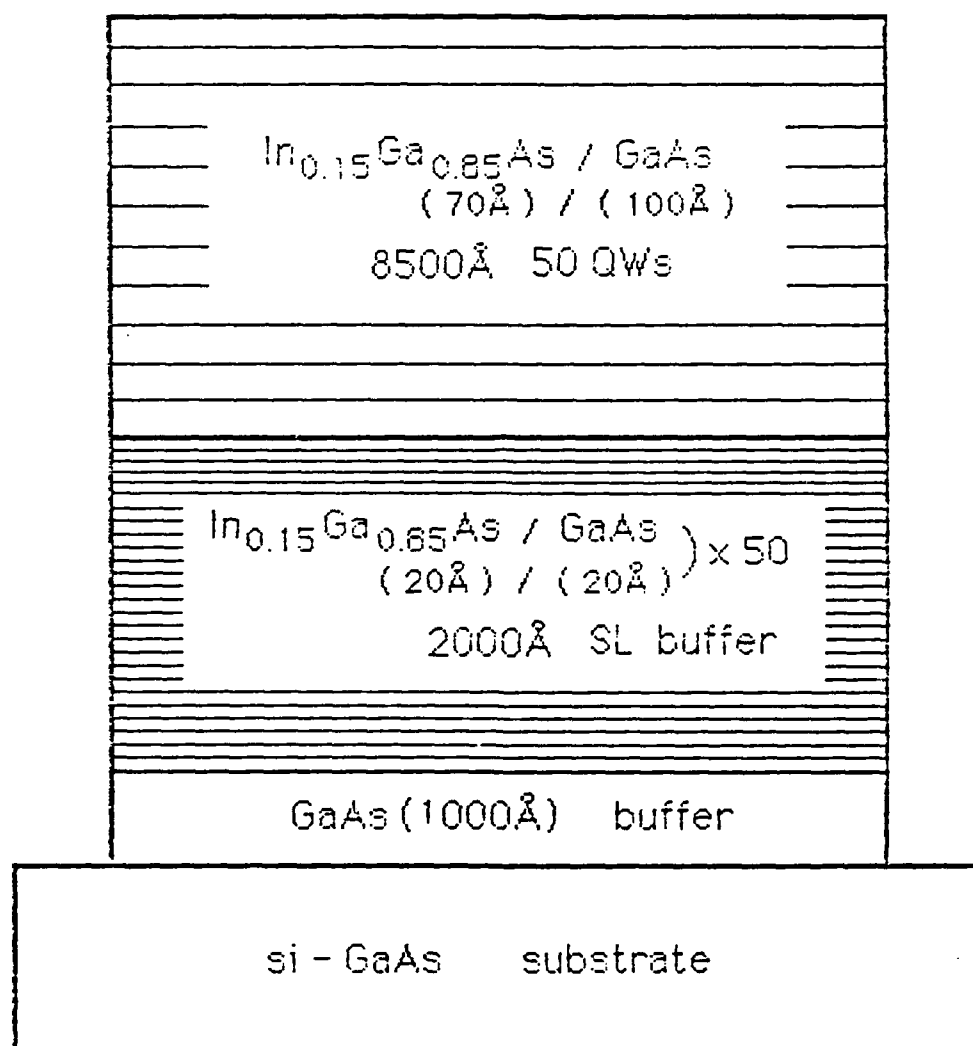


Fig. 9. Schematic of the sample MBE 572

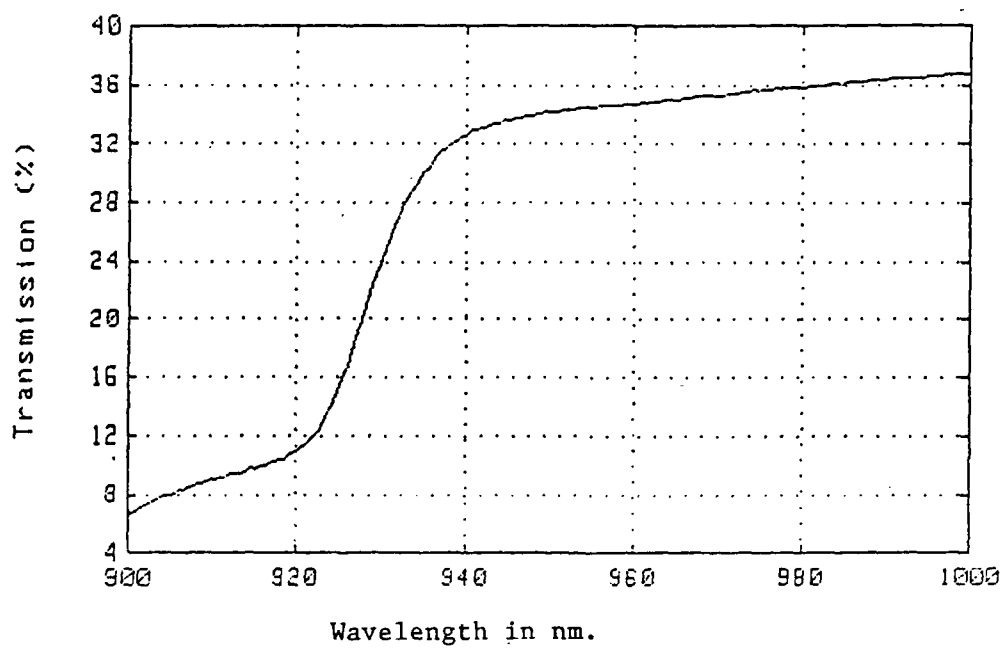


Fig. 10a. Transmission spectra of the superlattice (MBE 661)



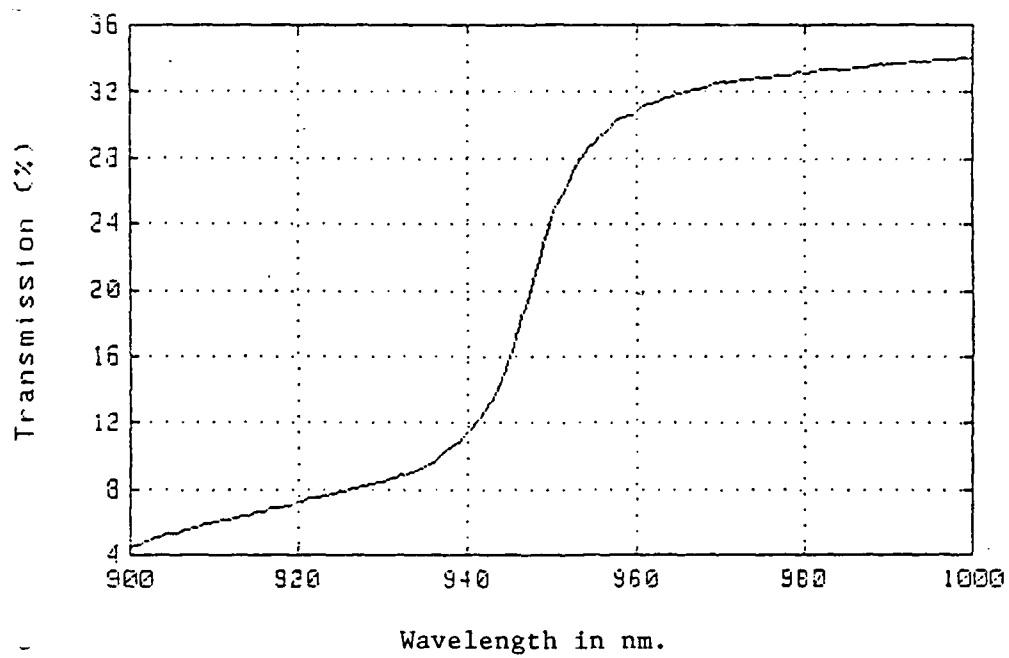


Fig. 10b. Transmission spectra of the superlattice (MBE 662).

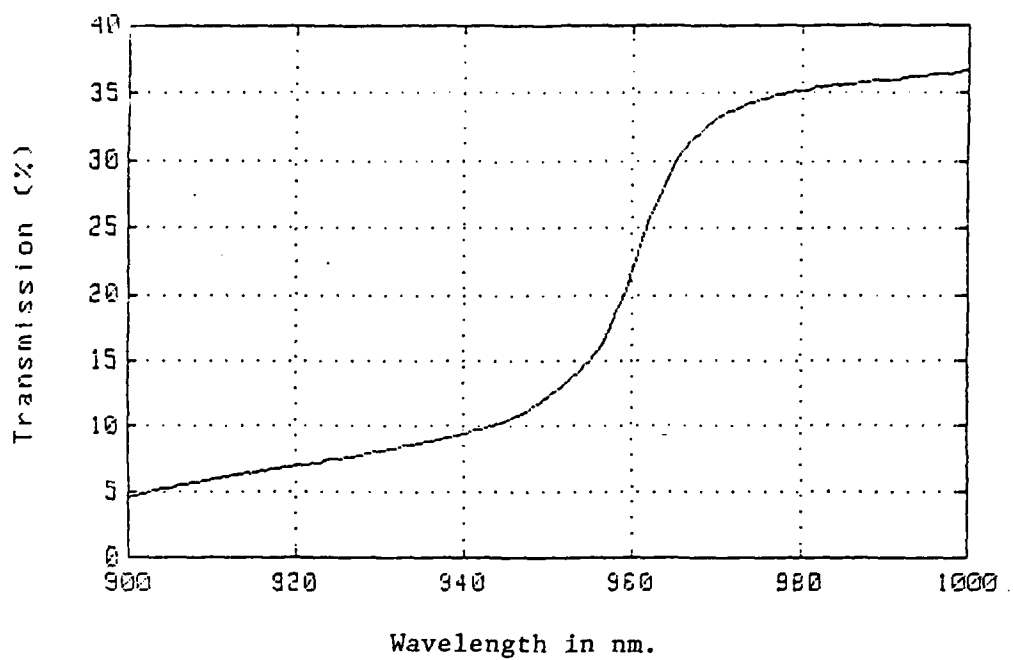


Fig. 10c. Transmission spectra of the superlattice (MBE 663)

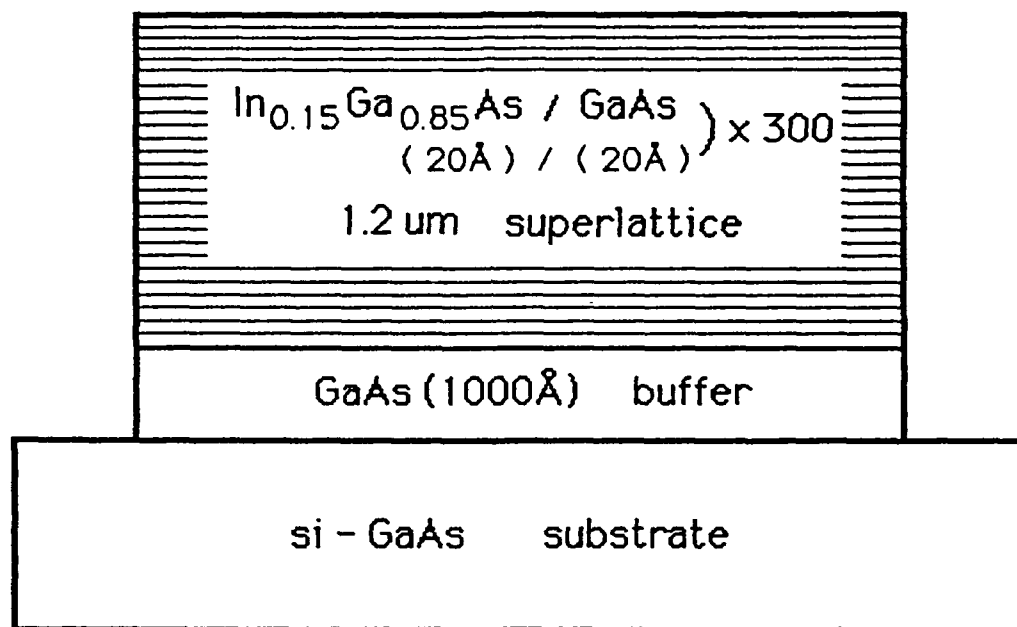


Fig.1L Schematic of the sample MBE 662

---

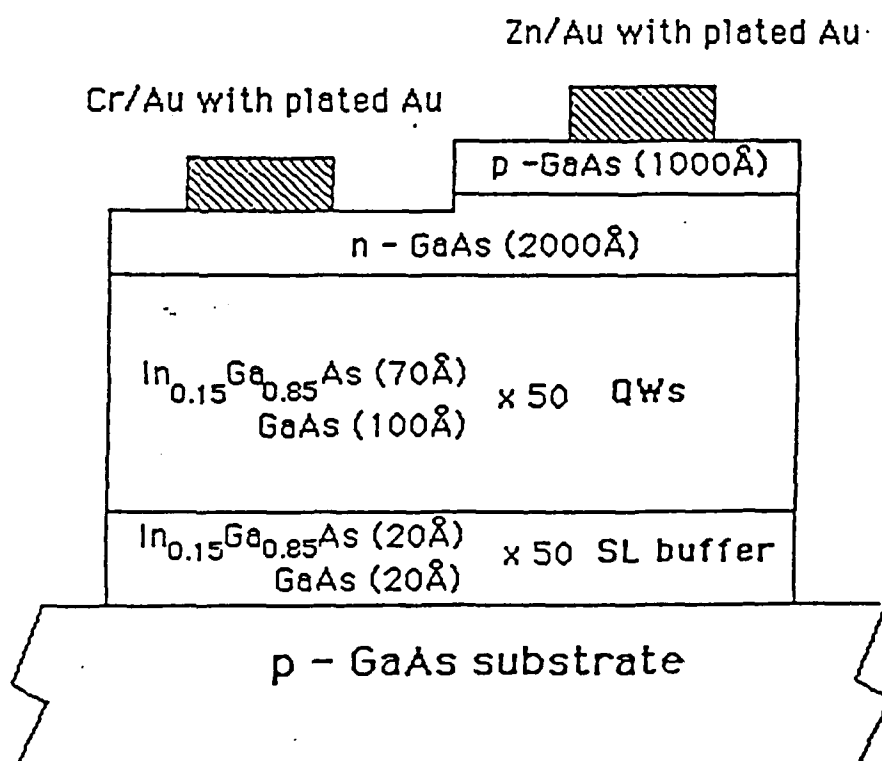
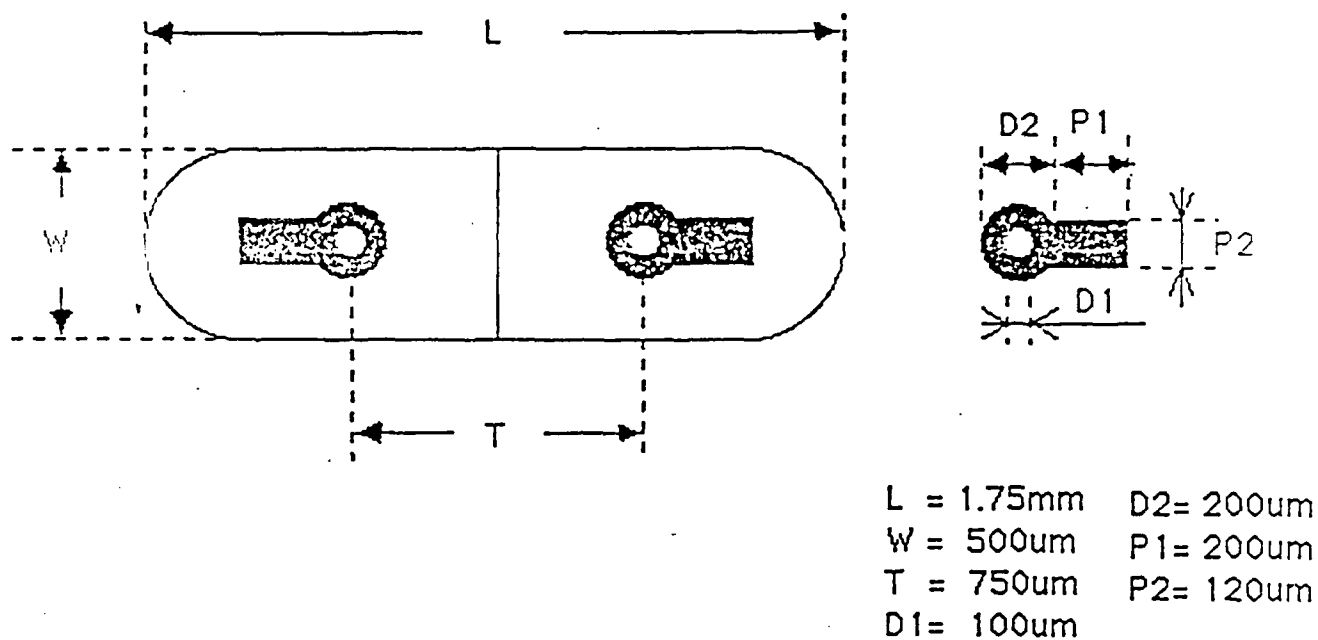
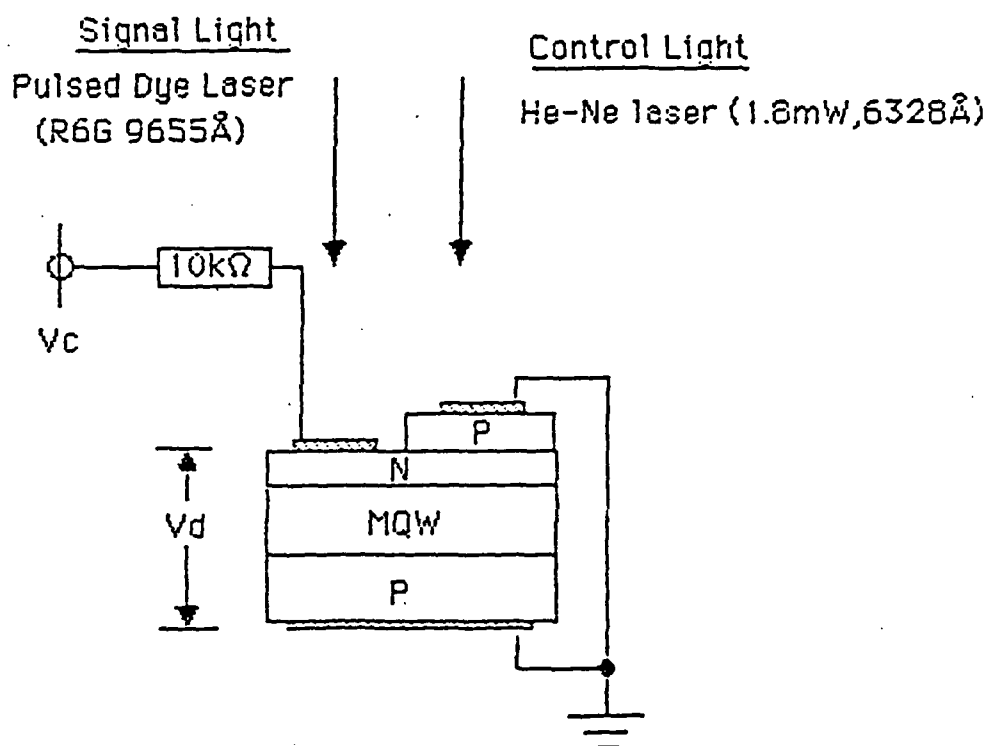


Fig.12. A p-n diode detector monolithically integrated with a n-i-p MQW modulator.



	$V_c$ (V)	$V_d$ (V)	-Log Trans (-ax)
W/O Light	5.0	4.8	0.2106
W Light	5.0	0.7	0.0578

Intensity Modulation (15.5%)

$$I_m = \exp ( 0.2016 - 0.0578 ) = 1.155$$

Fig. 13. Illustration of the experiment demonstrating the monolithically integrated detector/modulator pair.

# MBE533 Electroabsorption

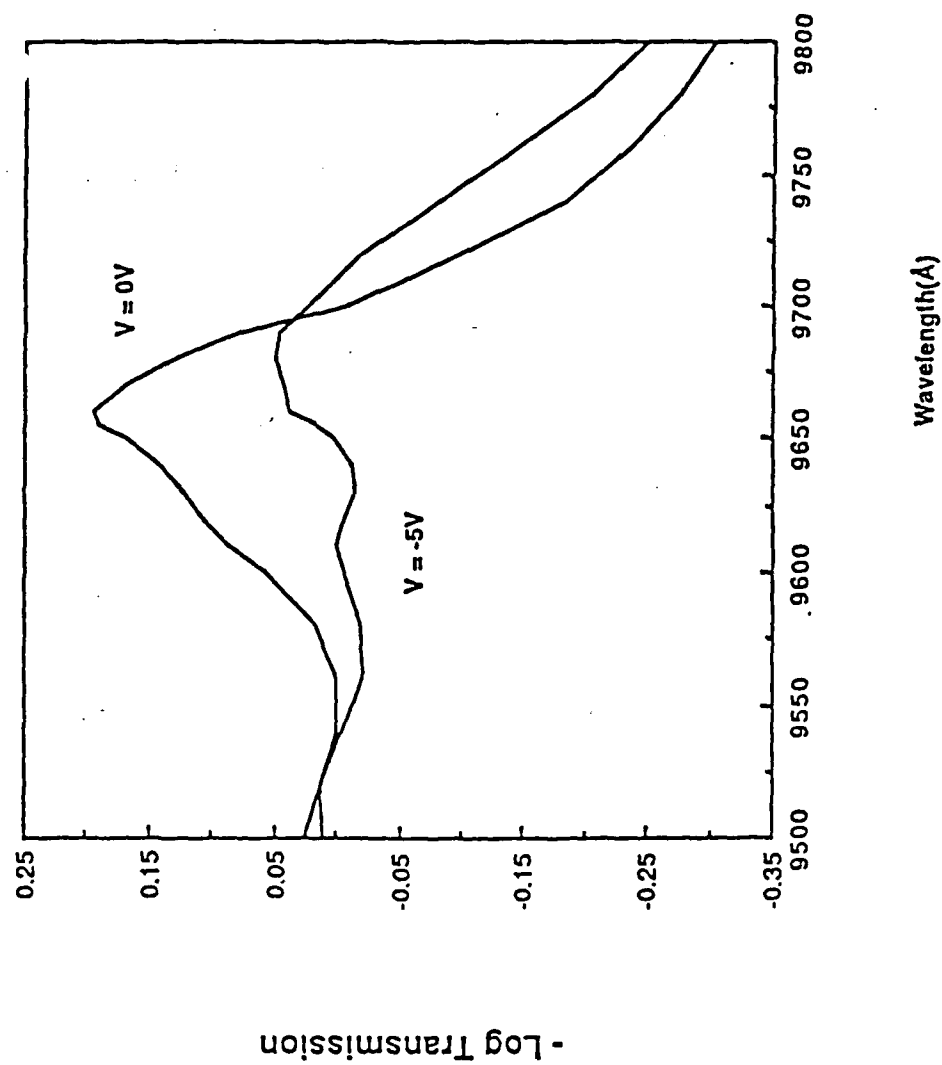


Fig. 14. The electro-absorption spectra of sample MBE-533.

# APPENDIX A

## A NEW SEMICONDUCTOR DEVICE - THE GATE-CONTROLLED PHOTODIODE: DEVICE CONCEPT AND EXPERIMENTAL RESULTS

C. C. Sun, H. H. Wieder, and W. S. C. Chang  
Department of Electrical and Computer Engineering, C-014  
University of California, San Diego  
La Jolla, California 92093

### Abstract

A new semiconductor device - the gate-controlled photodiode (GCPD) has been presented. Basically, the GCPD is a photodetector whose external quantum efficiency can be modulated by an applied gate voltage. In its linear region, the GCPD is a multiplier of the incident light intensity and gate voltage. Its potential applications include optical matrix multiplication, matrix inversion, etc. This device has been demonstrated experimentally in Si, but might be applied, as well, to compound semiconductors. Ten nanosecond response time and a nonlinearity of less than 3% within 30-dB range of light intensity and within 23-dB range of gate voltage have been obtained thus far.

## I. Introduction

Recently a new semiconductor device, the gate-controlled photodiode (GCPD), has been conceived and developed <sup>[1]</sup>, which can be incorporated in a two-dimensional (2-D) GCPD array where it may fulfill the combined function of an electrically addressed 2-D spatial light modulator (SLM) and a photodetector array. Potential applications are for optical signal processing and computing, such as optical matrix multiplication and matrix inversion.

Figure 1 illustrates schematically the GCPD. It consists of a p-n diode with its depletion region interconnected with the depletion region under a MOS gate. This gate is made of transparent material (e.g. poly-Si) while the p-n junction diode is covered by a metal electrode. If optical radiation at a wavelength shorter than the absorption edge of the semiconductor material is incident on the device, then photocurrent will be generated in the depletion region under the MOS gate. The function of the p-n junction diode is to collect the photocurrent. If the absorption length of the optical radiation in such a semiconductor is larger than the depletion depth  $X_d$ , as shown in Fig. 1, only the electron-hole pairs generated within the depletion region are converted into a photocurrent. The electron-hole pairs generated outside the depletion region will recombine, they do not contribute significantly to the photocurrent except by diffusion. Hence, for a substrate with short diffusion length, the photocurrent generated under the MOS gate is proportional approximately to the depletion depth  $X_d$ . For a MOS structure biased below its inversion threshold, the depletion depth  $X_d$  is controlled by the gate voltage  $V_G$ . Very few carriers are generated in the depletion region of the p-n junction diode because the radiation is blocked by the metal electrode. Thus, for reasonably long gates, the photocurrent  $I_{ph}$  is proportional, approximately, to the product of the light intensity  $I_o$  and the depletion depth  $X_d$



which, in turn, is a function of  $V_G$ .

It is assumed that in the depletion region along the direction parallel to the semiconductor-oxide interface there are drift and thermal diffusion of the charge carriers. This is different from conventional photodiodes in which drift is the dominant transport mechanism. Diffusion is slow, and it may limit the speed of response of the device. In order to increase the drift velocity, a special device structure using a stepped-oxide-thickness gate has been investigated experimentally in order to increase the transverse electric field.

In Section II the device physics of GCPD is described. Section III is concerned with the experimental device structure and its fabrication, and the experimental results are reported in Section IV. The potential applications are discussed briefly in Section V.

## II. The Device Physics

The basic physical structure of the GCPD is shown in Fig. 1. Although samples with p-type substrates have also been fabricated, we discuss here primarily devices fabricated on n-type substrates. The behavior of p-substrate devices is considered to be analogous to the n-substrate devices.

### II.1 Dark Current

Let the p-n junction diode be reverse biased at  $V_J$  while the gate voltage is negatively biased at  $V_G$ . In the absence of optical radiation, carriers are thermally generated in the semiconductor. The thermally-generated electron-hole pairs in both the gate depletion region and the p-n junction depletion region constitute the dark current.

According to the theoretical arguments of Grove and Fitzgerald, the total dark current,  $I_D$ , in a GCPD consists of three components: (1) The current generated in the p-n junction depletion region,  $I_{gen,J}$ , (2) The current generated in the gate depletion region,  $I_{gen,G}$ , and (3) The current generated in the surface layer of the gate depletion region,  $I_{gen,S}^{[2]}$ , i.e.

$$I_D = I_{gen,J} + I_{gen,G} + I_{gen,S}.$$

$I_{gen,J}$  and  $I_{gen,G}$  can be expressed in terms of the bulk generation rate and the volumes of the respective depletion regions. The surface generation current  $I_{gen,S}$  can be expressed in terms of the surface generation rate and the surface area of the depletion region. Thus,

$$I_{gen,J} = qUV_{JD},$$

$$I_{gen,G} = qUV_{GD},$$

and

$$I_{gen,S} = qU_s A_s,$$

where  $q$  is the electron charge,  $U$  is the bulk generation rate,  $U_s$  is the surface generation rate,  $V_{JD}$  is the volume of the p-n junction depletion region,  $V_{GD}$  is the volume of the gate depletion region, and  $A_s$  is the surface area of the gate depletion region.

Let the depletion depth under the MOS gate have a uniform value,  $X_d$ , then the dark current  $I_D$  may be expressed as  $I_D = qUV_{JD} + qU \cdot (A_s X_d) + qU_s A_s$ , which may be rewritten as

$$I_D = qUV_{JD} + qUA_s \left[ X_d + \frac{U_s}{U} \right]. \quad (1)$$

An estimate of the ratio  $U_s/U$  can be made on the basis of the Shockley-Read-Hall theory<sup>[3]</sup> of recombination-generation processes. Assuming that the effective capture cross-section of the bulk and surface trapping centers are the same, we may express this ratio as follows:

$$U_s/U = N_{st}/N_t, \text{ for single-level centers}$$

and

$$U_s/U = D_{st}/D_t, \text{ for uniformly-distributed centers,}$$

where  $N_t$  is the concentration of single level bulk recombination-generation centers,  $N_{st}$  is the density of single level surface centers,  $D_t$  is the concentration of uniformly-distributed bulk centers and  $D_{st}$  is the density of uniformly-distributed surface centers. For single level recombination-generation centers with energy level  $E_t = E_i$ , where  $E_i$  is the intrinsic Fermi level, or for uniformly-distributed recombination-generation centers within the forbidden gap, one obtains a simple result [2],

$$U_s/U = S_o T_o,$$

where  $S_o$  is the surface recombination velocity of a depleted surface, and  $T_o$  is the carrier lifetime within the depletion region. Typical values of  $S_o$  on thermally oxidized silicon surfaces are of the order of 1 to 10 cm/sec. Typical values of  $T_o$  are of the order of 1 to 10  $\mu$ sec [5]. Thus, typical values of  $S_o T_o$  are of the order of  $10^{-2}$  to 1  $\mu$ m.

## II.2 The Photocurrent

Equation (1) may be used to express photocurrent  $I_{ph}$  in the GCPD, provided that the thermal generation rates are replaced by photo-generation rates.

When a laser beam with power  $P_L$  illuminates the gate area  $A_g$  of the GCPD, the photo-generation rate in the semiconductor under the gate is given by [4]

$$G(x) = \eta \frac{\phi_o}{d} e^{-\frac{x}{d}}, \quad (2)$$

where  $d$  is the absorption length.  $\phi_o$  is the incident photon flux per unit area, given by  $\phi_o = P_L(1-\gamma)/A_s \cdot h\nu$ , where  $\gamma$  is the total fractional optical radiation loss of the structure due to the absorption and the reflection of the poly-Si gate and the oxide, and the reflection of the Si. The

photocurrent contributed by the gate depletion region is given by  $I_{ph,G} = q \int_{V_{GD}} G dv = q A_s \int_0^{X_d} G(x) dx$

. Thus, using Eq. (2), one may obtain

$$I_{ph,G} = \eta q \phi_o \left[ 1 - e^{-\frac{X_d}{d}} \right] \cdot A_s. \quad (3)$$

The carriers generated within a diffusion length outside the depletion region may also contribute to the photocurrent. If they are taken into account, Eq. (3) becomes [4]

$$I_{ph,G} = \eta q \phi_o \left[ 1 - \frac{\exp(-X_d/d)}{1 + L_p/d} \right] A_s, \quad (4)$$

where  $L_p$  is the hole diffusion length. For most cases,  $L_p < d$ , thus Eq. (4) reduces back to Eq. (3).

Under the assumption that the absorption in the depletion region is uniform, i.e.  $X_d \ll d$ , Eq. (3) becomes

$$I_{ph,G} = \eta q \frac{\phi_o}{d} \cdot (A_s X_d). \quad (5)$$

From Eq. (2), for  $X_d \ll d$ ,  $G = G_0 \approx \eta \frac{\phi_o}{d}$ . Thus, Eq. (5) may be rewritten as

$$I_{ph,G} = q G_0 (A_s X_d). \quad (6)$$

For thermal generation, the surface layer of a depletion region is considered to have a much higher generation rate than that of the bulk due to a much higher density of recombination-

generation centers at the surface layer. For optical generation, the role of recombination-generation centers is considered of no significance. Our experimental results also indicate that, for photoexcitation with photon energy slightly larger than the band gap of the semiconductor, the surface generation process is not important. Then, the total photocurrent  $I_{ph}$  in the GCPD may be expressed by Eq. (6), i.e.  $I_{ph} = I_{ph,G}$ . Note that the photo-generation rate in the p-n junction depletion region is negligible because the incident light is blocked by the metal electrode.

### IL3 The External Quantum Efficiency

The external quantum efficiency  $\eta_e$  is defined as the number of electron-hole pairs generated per incident photon, which contribute to the photocurrent [4],

$$\eta_e = (I_{ph}/q)/(P_L/h\nu). \quad (7)$$

It is usually convenient to measure experimentally the responsivity, which is defined here as the ratio of the photocurrent to the optical power [4],

$$R = \frac{I_{ph}}{P_L} = \frac{\eta_e q}{h\nu}. \quad (8)$$

From Eq. (6), one obtains  $I_{ph} = qG_o A_s X_d = \eta q \frac{\phi_o}{d} A_s X_d$ , which leads to

$$I_{ph} = P_L \frac{\eta q}{h\nu} \cdot \frac{X_d}{d}, \quad (9)$$

where we have neglected the total loss coefficient  $\gamma$ . Thus,

$$R = I_{ph}/P_L = \frac{\eta q}{h\nu} \cdot \frac{X_d}{d} \quad (10)$$

and

$$\eta_e = \frac{X_d \eta}{d}. \quad (11)$$

The gate voltage controls the depletion depth  $X_d$ , and the external quantum efficiency  $\eta_e$ .

#### II.4 The Depletion Depth $X_d$

The relationship between  $X_d$  and  $V_G$  depends on factors such as doping profile, oxide thickness, space charges in the oxide layer; these may be due to ionic contamination, or electrically active lattice defects, interface states, etc.

For a MOS structure, it is well known that <sup>[6]</sup>

$$V_G - V_{FB} = -\frac{\theta_s}{C_o} + \phi_s \quad (12)$$

where  $V_{FB}$  is the flat band voltage,  $\theta_s$  is the charge per unit area contained in the depletion layer of the semiconductor,  $C_o$  is the capacitance per unit area of the oxide layer, and  $\phi_s$  is the surface potential of the semiconductor. Under the depletion approximation and for a uniformly doped substrate,  $\phi_s$  is given by

$$\phi_s = -\frac{qN_D X_d^2}{2\epsilon_s \epsilon_o},$$

where  $N_D$  is the donor concentration,  $\epsilon_s$  is the dielectric constant of silicon, and  $\epsilon_o$  is the permittivity of free space,  $8.859 \times 10^{-14} \text{ F} \cdot \text{cm}^{-1}$ . For negative  $V_G$  when  $|V_G| \leq |V_T|$ , where  $V_T$  is the inversion voltage, we have

$$\theta_s = qN_D X_d,$$

then [6]

$$X_d = \frac{\epsilon_s \epsilon_o}{C_o} \left[ \left( 1 + \frac{2 |V_G - V_{FB}| C_o^2}{q N_D \epsilon_s \epsilon_o} \right)^{1/2} - 1 \right], \text{ for } |V_{FB}| \leq |V_G| \leq |V_T|. \quad (13)$$

Here  $C_o$  is given by

$$C_o = \frac{\epsilon_{ox} \epsilon_o}{X_o},$$

where  $X_o$  is the oxide layer thickness, and  $\epsilon_{ox}$  is the dielectric constant of  $SiO_2$ .

When  $V_G = V_T$ ,  $X_d$  will reach its maximum value,  $X_{d,max}$ . In the GCPD, there is a p-n junction interconnected with the MOS structure. Thus non-equilibrium MOS theory [2] should be used to estimate this value in order to take into account the effect of the p-n junction on the MOS structure. A good approximation of  $X_{d,max}$  for the short-gate GCPD is given by [2]

$$X_{d,max} = \left[ \frac{2 \epsilon_s \epsilon_o |V_J + 2\phi_F|}{q N_D} \right]^{1/2}, \quad (14)$$

where  $V_J$  is the junction voltage of the p-n junction diode, and  $\phi_F = (E_i - E_F)/q$ .  $E_F$  is the Fermi level of the semiconductor and  $E_i$  is the intrinsic Fermi level. Thus the dynamic range of  $V_G$  depends on  $V_J$ .

Equation (13) derived for no illumination is considered to be still valid when the density of the photo-generated carriers is much smaller than  $N_D$  [7].

## II.5 Transport Mechanisms

In the depletion region under the gate, when electron-hole pairs are generated by optical radiation, the electric field separates them, and the electrons and holes drift in opposite directions.

In a GCPD with n-type substrate and biased negatively, all photo-generated electrons may drift

toward the grounded substrate to contribute to the photocurrent measured in the external circuit. The hole transport mechanism, however, is more complicated. In the gate depletion region, photo-generated holes transfer in the transverse direction parallel to the semiconductor-oxide interface toward the p-n junction. Only those holes, which reach the p-n junction, contribute to the photocurrent. In a MOS structure not connected to a p-n junction diode, there is only a longitudinal electric field in the direction normal to the semiconductor-oxide interface. In the GCPD, the transverse electric field generally is weak except for the region near the p-n junction. Hence, diffusion plays an important role in hole transport.

Suppose the transverse electric field  $E_y$  is zero everywhere under the gate oxide except at  $y \equiv L$ . In that case, the gradient of the hole concentration along the  $y$  direction is small at  $y \equiv 0$ . At  $y = L$ , there is a strong  $E_y$  that produces a large drift velocity, thus the hole concentration is low. Transport of holes along the  $y$  direction can then be modeled by the solution of the diffusion equation subject to the following boundary conditions: Zero hole gradient at  $y = 0$  and zero hole concentration at  $y = L$ . Such a solution had been obtained by Carnes et al. [8]. From this solution, one may obtain the total number of holes remaining at time  $t$ ,  $N_{tot}(t)$ , in the depletion region under the gate oxide as [8]

$$N_{tot}(t) = \frac{8}{\pi^2} N_{tot}(0) \exp\left[-\frac{t}{\tau_d}\right] \quad (15)$$

where  $\tau_d = 4L^2/\pi^2 D_p$ ,  $D_p$  is the hole diffusion constant. Equation (15) implies that the decay of the photo-generated holes in the depletion region under the gate due to diffusion alone is exponential in time with decay constant  $\tau_d$ . The calculated  $\tau_d$  versus gate length  $L$ , for both n- and p-substrate, are shown as dashed curves in Fig.2.



In reality, the drift also plays a role in hole transport in the GCPD. In the cases of short-gate devices or stepped-gate oxide devices, the drift mechanism will dominate. The value of  $4L^2/\pi^2 D_p$  is only the upper limit of the response time in a GCPD. An investigation on transport mechanisms based on solving 2-D Poisson's equation and continuity equations will be reported elsewhere.

### III. Device Structure and Fabrication

GCPDs with poly-Si gates have been fabricated on both n- and p-type silicon substrates. Figure 3 shows the structure of the GCPD as actually implemented. Figure 4 shows a top-view photomicrograph of a GCPD sample with 75- $\mu\text{m}$  gate length. The experimental GCPD incorporates the major features of the structure shown in Fig. 1 with some modifications. One modification is the use of an  $n^-/n^+$  epitaxial substrate, another modification is the use of an  $n^+$ -doped ring. The objective of the modifications is to minimize series resistance. The 150  $\mu\text{m}$  thick  $n^+$ -substrate is phosphorus-doped with doping concentration  $N_D = 1 \times 10^{19} \text{ cm}^{-3}$  (0.006  $\Omega$ -cm resistivity), while the 15  $\mu\text{m}$  thick  $n^-$ -epitaxial layer has  $N_D = 4 \times 10^{14} \text{ cm}^{-3}$  (11 - 12  $\Omega$ -cm resistivity). These epitaxial wafers are <100>-oriented. Gate lengths are 75  $\mu\text{m}$ , 35  $\mu\text{m}$ , 25  $\mu\text{m}$ , and 15  $\mu\text{m}$ .

The fabrication procedure started with the cleaning of silicon wafers. A 1- $\mu\text{m}$ -thick field oxide was thermally grown by the wet oxidation process at 1050degreeC and then selectively etched in buffered HF to define the  $n^+$ -ring area. After the  $n^+$ -ring was formed by phosphorus diffusion, a gate-oxide of 1000angstrom was then grown in dry  $O_2$  at 1100degreeC on the gate area. Then the 5000angstrom thick poly-Si was deposited at 625degreeC by LPCVD. The poly-Si gate was patterned by photolithography and plasma etching. Boron diffusion was carried out

simultaneously for both the  $p^+$ -region of the p-n junction diode and the poly-Si gate - this is a so-called "self-alignment diffusion process". After high-temperature annealing in Ar at 1000degreeC for 30 min, the contact windows were opened and the Al electrodes were formed. Then, the samples were annealed in forming gas (10% hydrogen and 90% nitrogen) at 450degreeC for 30 min.

After the above process, the density of the fixed oxide charge was determined to be about  $3 \times 10^{10} \text{ cm}^{-2}$ , and the interface state density was determined to be less than  $2.5 \times 10^{10} \text{ cm}^{-2}$ , from the C-V measurements. The flat-band voltages  $V_{FB}$  were determined to be -0.3 V to -0.5 V.

#### IV. Experimental Measurements

##### IV.1 The Experimental Evaluation Setup

The experimental setup is illustrated in Fig. 5. A cw semiconductor laser with 0.84- $\mu\text{m}$  wavelength is used as the light source. Its maximum output power is 5.5 mw, and its response time is 1 ns. The relationship between electrical current input and optical output of the semiconductor laser was calibrated accurately. The gate voltage  $V_G$  of the GCPD is defined as the voltage between the gate and the substrate and was supplied by either a D.C. source or a pulse generator. The photocurrent  $I_{ph}$  is measured through a sampling resistor  $R_o$ .

##### IV.2 Responsivity and Photocurrent

If we neglect the surface photo-generation current and the diffusion of the carriers into the depletion region from the substrate, the responsivity  $R$  and the photocurrent  $I_{ph}$  of the GCPD are given by Eqs. (9) and (10). The dependence of  $X_d$  on  $V_G$  is given by Eq. (13). Combining Eq.

(13) with Eq. (9), we obtain the dependence of  $I_{ph}$  on both  $P_L$  and  $V_G$ :

$$I_{ph} = \frac{\eta q}{h\nu} \cdot \frac{P_L}{d} \cdot \frac{\epsilon_s \epsilon_o}{Co} \left[ \left( 1 + \frac{2|V_G - V_{FB}| Co^2}{qN_D \epsilon_s \epsilon_o} \right)^{1/2} - 1 \right], \text{ for } |V_{FB}| \leq |V_G| \leq |V_T|. \quad (16)$$

The computed curves of  $I_{ph}$  versus  $P_L$ ,  $V_G$  as a parameter, are shown in Fig. 6 and Fig. 7. Equation (16) is valid for substrates with uniform doping profile when the effect of the  $p^+$  region on the depletion region under the gate can be neglected. Figure 6 also shows the experimental data for the 75- $\mu\text{m}$  gate-length GCPD. For  $V_G \leq -2V$ , the data agree with Eq. (16) well. In Fig. 7, for the 25- $\mu\text{m}$  gate-length sample, the experimental data deviates from Eq. (16) for  $V_G > -10$  V. This deviation is attributed, in part, to the effect of  $p^+$  region on the depletion region under the gate. In the case of shorter gate length, one-dimension approximation is no longer valid, and two-dimension analysis must be used.

Figure 8 shows the calculated and the measured responsivity  $R$  versus  $V_G$  for 75- $\mu\text{m}$ , 35- $\mu\text{m}$  and 25- $\mu\text{m}$  gate-length samples, respectively. Note that the measured responsivity is not zero at zero gate-voltage for all the samples. When  $V_G = 0$ , there is no depletion layer under the gate. Probably the zero-gate-voltage photocurrent,  $I_{ph,0}$ , is due to the carriers generated near the p-n junction within a hole-diffusion length range as illustrated in the inset in Fig. 9. In order to verify this explanation, let the gate width be unity, then we have

$$I_{ph,0} = qG_o \cdot L_p(X_j + w),$$

where  $L_p$  is the hole diffusion length,  $X_j$  is the junction depth, and  $w$  is the depletion depth of the p-n junction. Assuming uniform absorption, we obtain

$$G_o = \eta \frac{\phi_o}{d} = \frac{\eta}{d} \frac{P_L}{A_s \cdot h\nu}$$

Here  $A_s = L$ . Thus

$$I_{ph,o} = \frac{\eta q}{h\nu} \cdot \frac{L_p(X_j+w)}{L \cdot d} \cdot P_L$$

and

$$R_o = \frac{I_{ph,o}}{P_L} = \frac{\eta q}{h\nu} \cdot \frac{L_p(X_j+w)}{L \cdot d} \quad (17)$$

Taking  $L_p = 5 \mu\text{m}$ ,  $X_j+w = 12 \mu\text{m}$ , we obtain the curve of  $R_o$  versus  $L$ , shown in Fig. 9. The experimental data, plotted as solid circles, are in agreement with the theoretical curve.

Figure 10 shows a plot of  $I_{ph}$  versus  $V_G$ , with  $P_L$  as a parameter, for  $L = 25 \mu\text{m}$ . The linearity of the experimental data, for both  $I_{ph}$  versus  $P_L$  and  $I_{ph}$  versus  $V_G$ , has been determined based on the data. Using the method of least squares, we find straight lines which are able to fit the experimental data best, and then calculate the deviations of the experimental data from these lines. For 15- $\mu\text{m}$  and 25- $\mu\text{m}$  gate length samples, within the ranges of the light intensity  $I_o$  from 2  $\text{mw/cm}^2$  to 2000  $\text{mw/cm}^2$ , and  $V_G$  from 0.1 V to 20 V, the mean relative deviation is less than 3% for both the relationships of  $I_{ph}$  versus  $P_L$ , and  $I_{ph}$  versus  $V_G$ . For 35- $\mu\text{m}$  and 75-  $\mu\text{m}$  gate length samples, the mean relative deviations are 3.8% and 5.5%, respectively.

In the case of thermally generated carriers, when the surface is depleted, recombination-generation centers at the oxide-silicon interface provide yet another contribution to the total generation current. There is a sharp jump in the total thermally generated current versus gate voltage characteristics <sup>[5]</sup>. However, no such leap in the  $I_{ph}$  versus  $V_G$  characteristics has been observed for the  $\lambda = 0.84 \mu\text{m}$  light incident on the Si GCPD (see Fig. 10).

### IV.3 Response Time

Both optical and electrical response times of GCPD samples were measured. Here the rise time is defined as the time within which the electrical output of the GCPD (i.e.  $-I_{ph}R_o$  in Fig. 5) reaches the  $\frac{e-1}{e}$  ( $\approx 0.63$ ) of its maximum value for an optical or electrical square pulse input, while the decay time is defined as the time after which the output of the GCPD decays to the  $\frac{1}{e}$  ( $\approx 0.37$ ) from its maximum value. In our experiment, the decay time is equal to the rise time approximately.

Figure 2 shows the experimental data of optical response time (solid circles and triangles), for GCPD devices with different gate lengths, on both n- and p-type substrates. Obviously, the response time depends on the minority carrier mobility and the gate length. For longer-gate devices, the experimental data are closer to the calculated time-constant curves based on diffusion.

Generally speaking, the transverse electric field is weak in a GCPD, as discussed previously. In order to increase the transverse electric field, the devices with stepped gate-oxide have been made. Preliminary results indicate one-order-of-magnitude improvement in response time.

Figure 2 also shows the experimental data of the electrical response time (hollow circles and triangles). In this case the optical power is kept constant while the gate voltage is in the form of electrical square pulses. Significant differences between electrical response and optical response may be observed only for 15- $\mu\text{m}$ -gate-length samples. This difference is attributed to the additional RC time constant which is used to establish the depletion region. This RC time constant should be added to the carrier transit time. Hence, the response time of the electrical

pulse is greater than that of the optical pulse. In the GCPDs with  $n^- - n^+$  or  $p^- - p^+$  epitaxial substrates, the RC time constants are on the order of several ns. For GCPD devices with response times greater than a hundred nanosecond, this difference cannot be observed.

#### IV.4 Dynamic Range

The dynamic range of  $V_G$  of a GCPD will be limited by the saturation of R at large negative gate voltage at the upper end and by the nonzero R at  $V_G$  near zero at the lower end.

In the depletion approximation, the maximum value of the depletion depth  $X_d$  is given by [2]

$$X_{d,max} = \left[ \frac{2\epsilon_s \epsilon_o |V_J + 2\phi_F|}{qN_D} \right]^{1/2}.$$

The gate voltage at which  $X_d$  reaches this value is defined as the inversion voltage,  $V_T$ . The starting point of depletion under the gate oxide is at  $V_G = V_{FB}$ . Hence, Eq. (16) is valid only within the range of  $V_G$  given by

$$|V_{FB}| \leq |V_G| \leq |V_T|,$$

where  $V_T$  is a function of  $V_J$ . In principle, this range may be defined as the ultimate limit of the dynamic range of  $V_G$ .

For the upper limit, as  $V_G$  reaches  $V_T$ ,  $V_G$  can no longer control  $X_d$ . R will be saturated at  $V_G = V_T$ . The calculated curves of R versus  $V_G$ , using  $V_J$  as a parameter and the experimental measurements are shown in Fig. 11. Basically, the experimental data agrees with the above prediction. However, it is apparent that the experimentally measured R continues to increase at gate voltages which are more negative than the calculated  $V_T$ . For example, for the 25- $\mu\text{m}$  gate-length sample, the calculated  $V_T$  is -22.5 V for  $V_J = -20$  V, but R is absolutely independent of  $V_G$

only for  $V_G \leq -40$  V.

On the other hand, for the lower limit, the flat-band voltage,  $V_{FB}$ , has been determined to be -0.3 V to -0.5 V by C-V measurement. Usually,  $X_d$  is considered to be zero at  $V_G = V_{FB}$ . However, we have observed a photocurrent at  $V_G = 0$ , as discussed in section IV.2.

The detectable minimum optical power is 0.02  $\mu$ w for 75-  $\mu$ m gate length sample, which corresponds to the light intensity of 50  $\mu$ w/cm<sup>2</sup>.

## V. Potential Applications

Within the range of  $V_G$  where  $X_d$  is approximately linearly dependent on  $V_G$ , the GCPD is, in effect, a multiplier of  $P_L$  and  $V_G$ . Thus, an optical matrix-vector multiplier based on a GCPD array may be obtained <sup>[1]</sup>. Furthermore, such a 2-D GCPD array may serve as a building block for other optical processors, such, for example, a matrix inverter.

A 2-D GCPD array may be used for matrix-vector multiplication as follows. Consider the 2-D array shown in Fig. 12, which consists of  $N \times N$  GCPDs. At each row, the  $p^+$  doped regions of adjacent GCPDs are interconnected to each other via a  $p^+$  collector bar. There are thin gate-oxide layers over the gate region close to each  $p^+$  bar, and thick-oxide layers between adjacent gates in different rows. At each column, the same poly-Si gate strip is deposited over both the thin oxides and the thick oxides. The voltage applied to the poly-Si gate strip induces depletion layers under all the gates in the same column. The thick-oxide layers are thick enough so that there are essentially no depletion layers formed under the thick-oxide layers in the normal operating range of the gate voltage. Let  $A_{ij}$  be the optical intensity incident on the GCPD at the  $i$ th row and the  $j$ th column and  $X_j$  be the gate voltage applied to the  $j$ th column. All the devices in the  $i$ th row use the same  $p^+$  collector bar, thus the photocurrent at the  $i$ th row is proportional to

$\sum_{j=1}^N A_{ij} X_j$ . Let  $Y_i$  be this photocurrent. If  $\vec{A}$  is the 2-D optical input,  $\vec{X}$  is the input vector,

represented by the gate voltages, then  $\vec{Y}$  is the product vector, i.e.

$$\vec{Y} = K \vec{A} \cdot \vec{X},$$

where  $K$  is a constant of proportionality. Thus, the GCPD array is capable of performing the basic matrix-vector multiplication operations.

A major feature of a GCPD matrix processor is its high parallelism. In such a processor, the signal detection, multiplication and addition are carried out simultaneously. The interconnection of the various GCPDs for obtaining the summation of photocurrents in a row and applying the identical  $V_G$  to all the devices in the same column is extremely simple. Thus, a large array can be fabricated in a fairly simple manner. These two features might allow operations to be carried out with high speed on large matrices.

The GCPD array might also be used as non-matrix processors, such as a generalized crossbar switching network.

## VI. Conclusion

A new semiconductor device, the gate-controlled photodiode, has been experimentally demonstrated. In this device, the gate voltage  $V_G$  controls the depletion depth  $X_d$  and modulates the photocurrent. Thus, in the linear region, its photocurrent is proportional to the product of the gate voltage and the light intensity. Based on the depletion approximation and a one-dimensional model, a simple device model has been presented. The experimental data agree with the theoretical predicted performance based on this simple model.



By choosing the proper doping concentration and lifetime of the carriers in the substrate and the oxide thickness. GCPD samples with ten-nanosecond response time, and non-linearity of less than 3% within 30-dB range of light intensity and within 23-dB range of gate voltage have been obtained. The response speed, the linearity, and the dynamic range may be improved in the future by further optimizing the design of the GCPD. For example, non-uniform doping profile may be utilized to improve the linearity of the dependence of  $I_{ph}$  on  $V_G$ . On the other hand, it is also possible to design a GCPD structure that has more enhanced nonlinear characteristics.

A 2-D GCPD array may be used in some applications such as matrix inversion to serve the function of the 2-D SLM and the photodetector array. It has a higher speed than that of presently available 2-D SLMs. It may play an active role in optical signal processing and computing.

#### Acknowledgment

This work was supported in part by AFOSR Grant No. 84-0389.

#### References

1. C.C. Sun, W.S.C. Chang and H.H. Wieder, "The gate-controlled photodiode for optical matrix multiplication applications", *Proc. SPIE*, Vol. 698, 207-210 (1986).
2. A.S. Grove and D.J. Fitzgerald, "Surface effects on p-n junctions: Characteristics of surface space-charge regions under non-equilibrium conditions", *Solid-State Electronics*, Vol. 9, 783-806 (1966).
3. R.N. Hall, "Electron-hole recombination in germanium", *Physical Review*, Vol. 87, 387 (1952); W. Shockley and W.T. Read, Jr., "Statistics of the recombinations of holes and electrons", *Physical Review*, Vol. 87, 835-842 (1952).

4. S.M. Sze, *Physics of Semiconductor Devices*, 2nd ed. New York:Wiley,1981.
5. A.S. Grove, *Physics and Technology of Semiconductor Devices*, New York:John Wiley & Sons,1967.
6. S.M. Sze, *Physics of Semiconductor Devices*, New York:Wiley,1969.
7. J. Grosvalet and C. Jund, "Influence of illumination on MIS capacitance in the strong inversion region", *IEEE Trans. Electron. Devices*, Vol. ED-14, 777-780 (1967).
8. J.E. Carnes, W.F. Kosonocky and E.G. Ramberg, "Free charge transfer in charge-coupled devices", *IEEE Trans. Electron Devices*, Vol. ED-19, 798-808 (1972).

### Figure Captions

- Figure 1. A schematic diagram of the gate-controlled photodiode (GCPD).
- Figure 2. Response time  $\tau$  versus gate length  $L$  for both  $n$ - and  $p$ -type substrates. Here  $D_n = 18.3 \text{ cm}^2 \cdot \text{S}^{-1}$  and  $D_p = 6.5 \text{ cm}^2 \cdot \text{S}^{-1}$ .
- Figure 3. Cross-section of the gate-controlled photodiode (GCPD) with poly-Si gate.  $N^-$  on  $N^+$  epitaxial structure and  $N^+$  ring are used to reduce the series resistance.
- Figure 4. A 200X photomicrograph of a GCPD sample (gate length  $L = 75 \mu\text{m}$ ).
- Figure 5. A schematic diagram of the experimental setup.
- Figure 6. Photocurrent  $I_{ph}$  versus optical power  $P_L$ ,  $V_G$  as a parameter, for  $75\text{-}\mu\text{m}$  gate length GCPD.
- Figure 7. Photocurrent  $I_{ph}$  versus optical power  $P_L$ ,  $V_G$  as a parameter, for  $25\text{-}\mu\text{m}$  gate length GCPD.
- Figure 8. Responsivity  $R$  versus gate voltage  $V_G$  for different gate-length GCPDs.
- Figure 9. Comparison of the experimental data of  $R_o$  with the calculated curve based on the simple model shown in the insert.
- Figure 10. Photocurrent  $I_{ph}$  versus gate voltage  $V_G$ , optical power  $P_L$  as a parameter. Gate length  $L = 25 \mu\text{m}$ .
- Figure 11. Responsivity  $R$  versus gate voltage  $V_G$  for different junction voltages.
- Figure 12. A top view of the proposed GCPD matrix-vector multiplier.

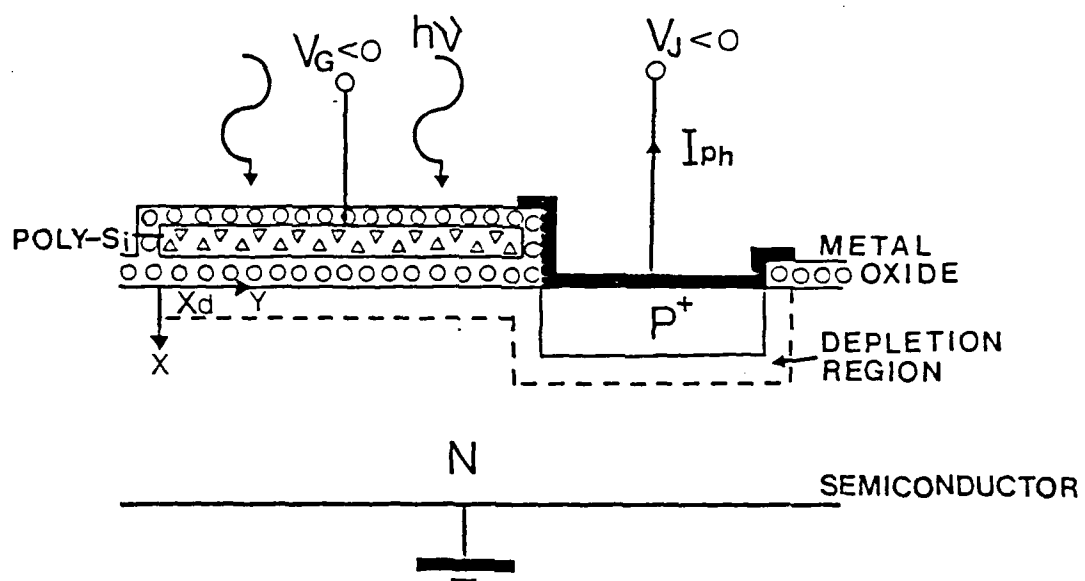


Fig. 1

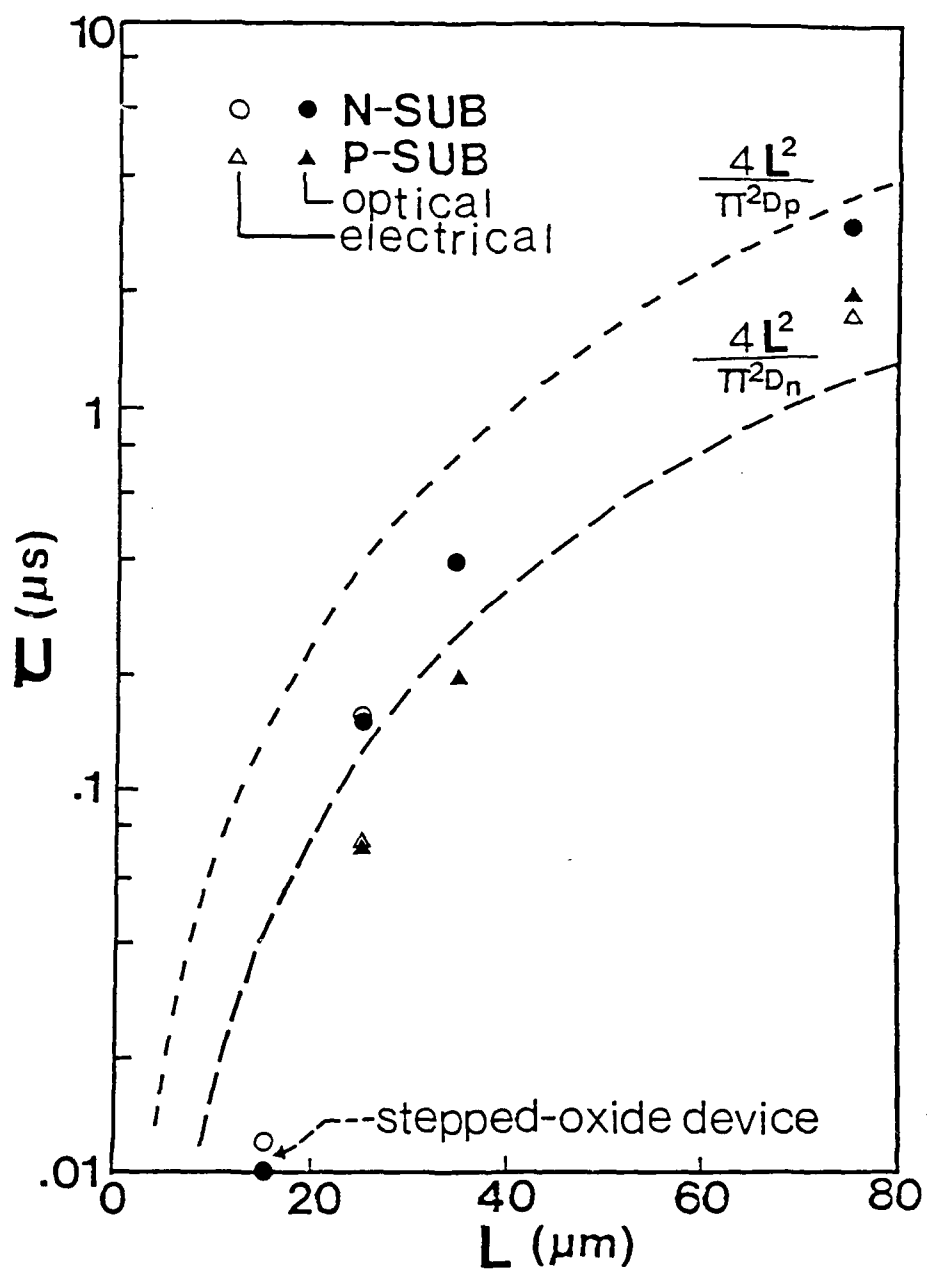


Fig. 2

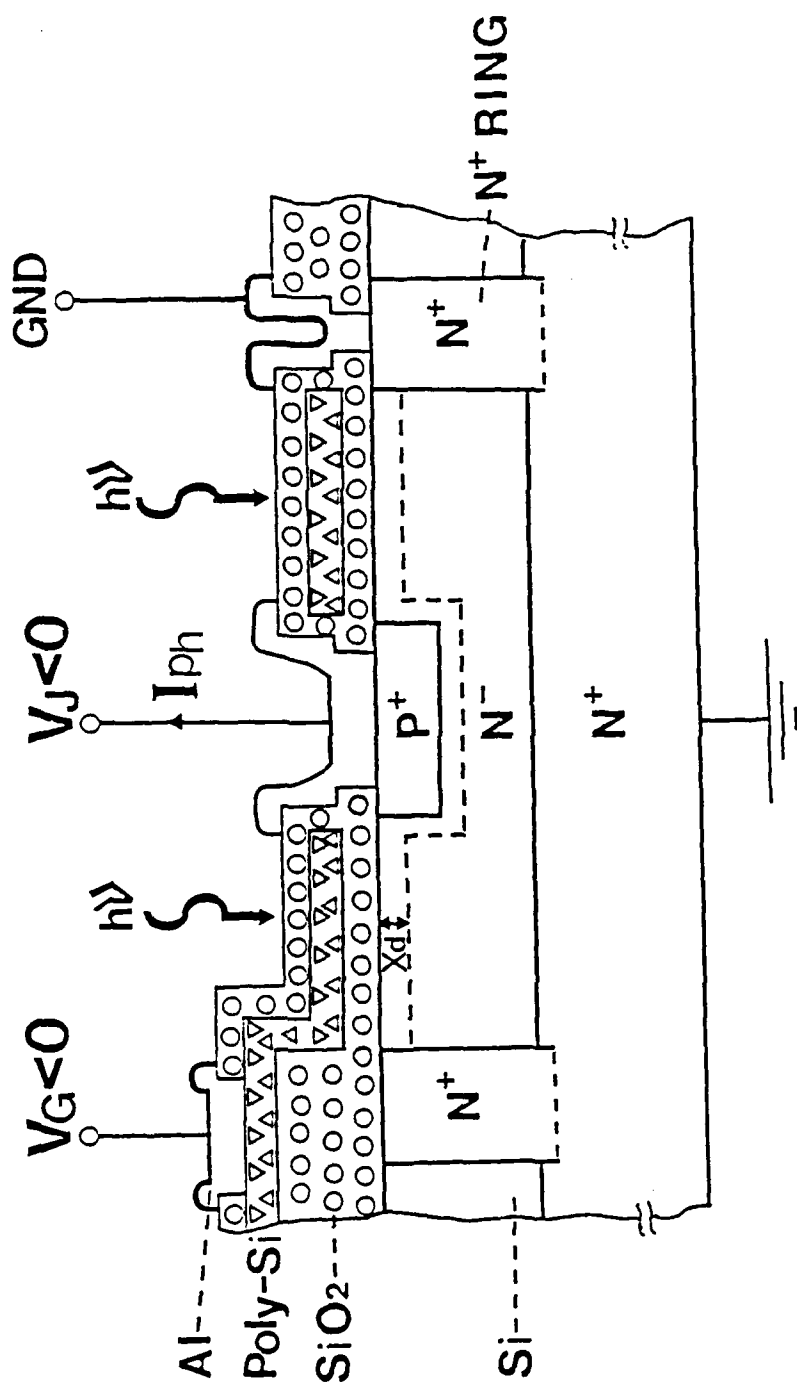


Fig. 3

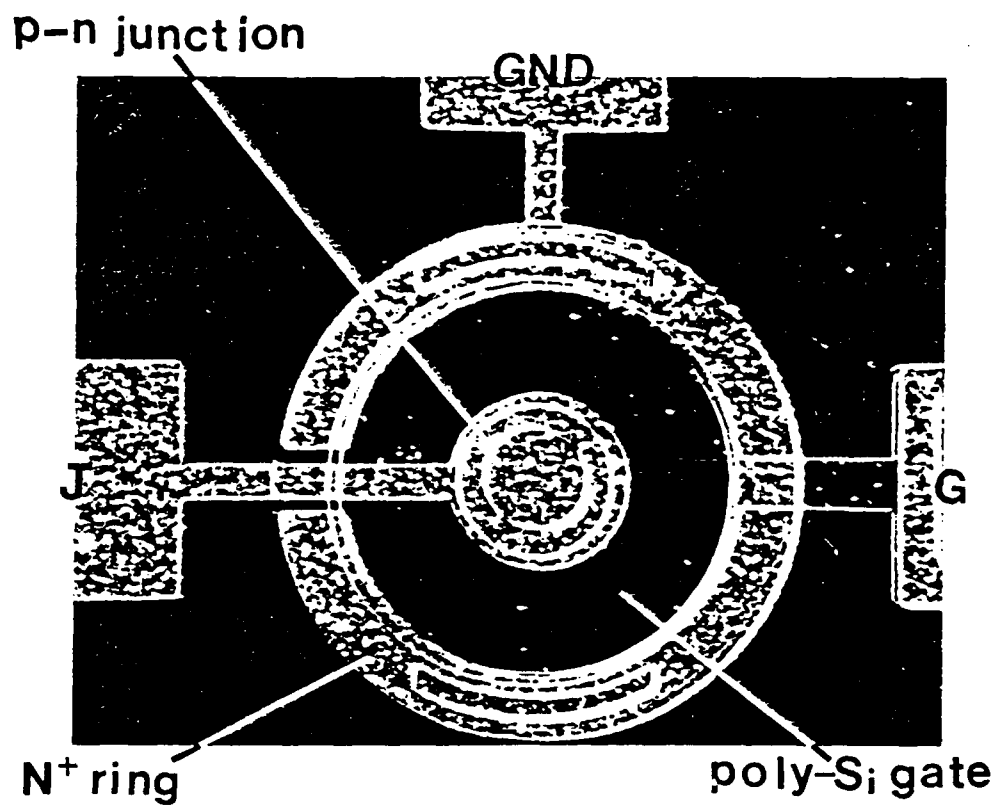


Fig. 4

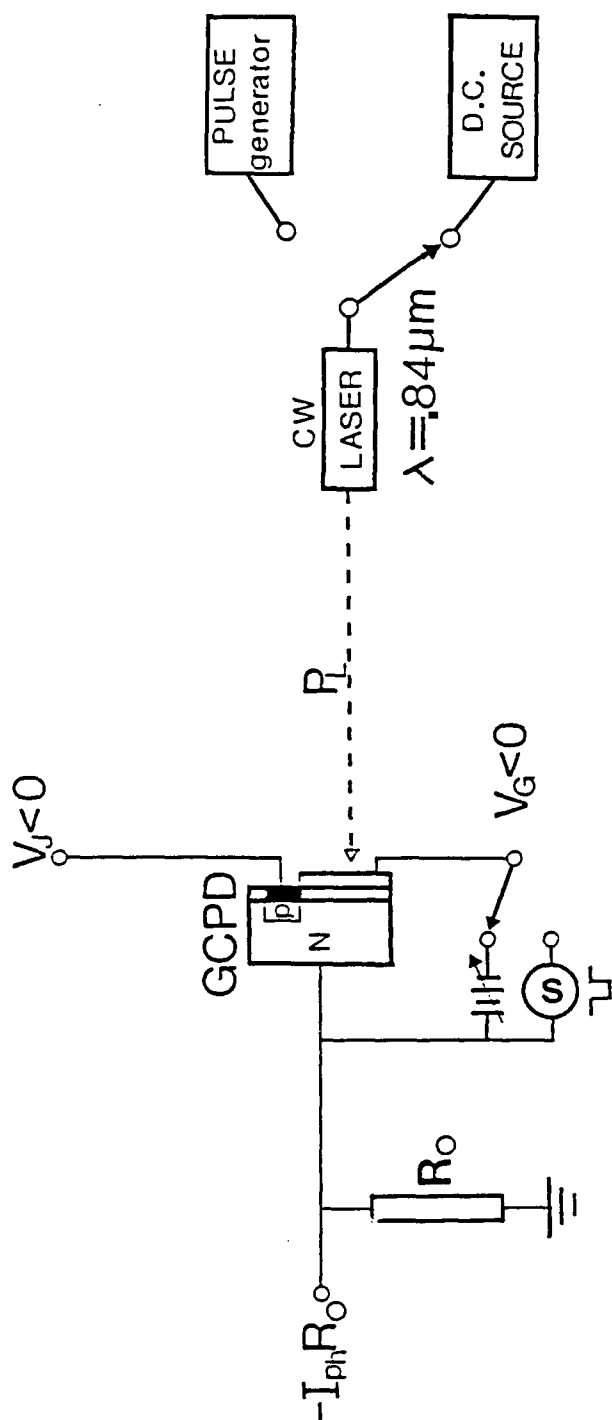


Fig. 5



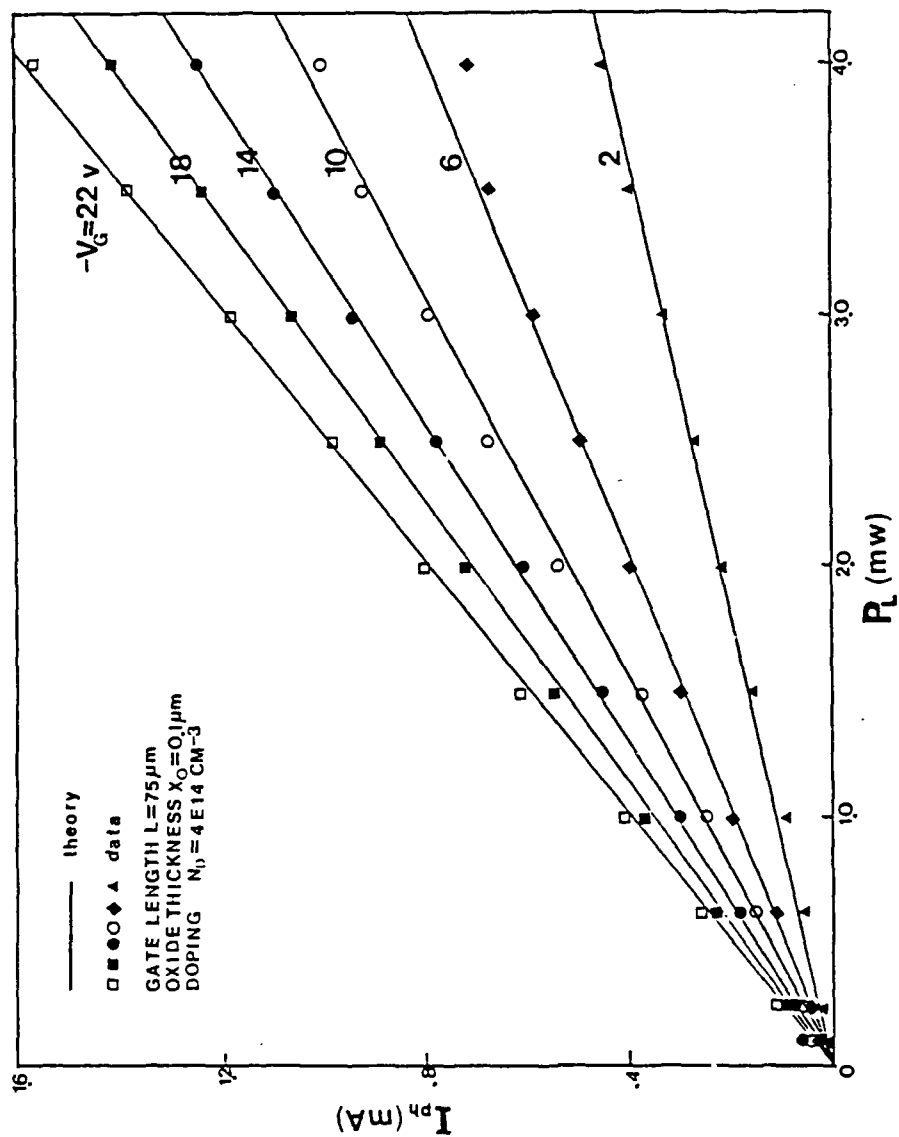


Fig. 6

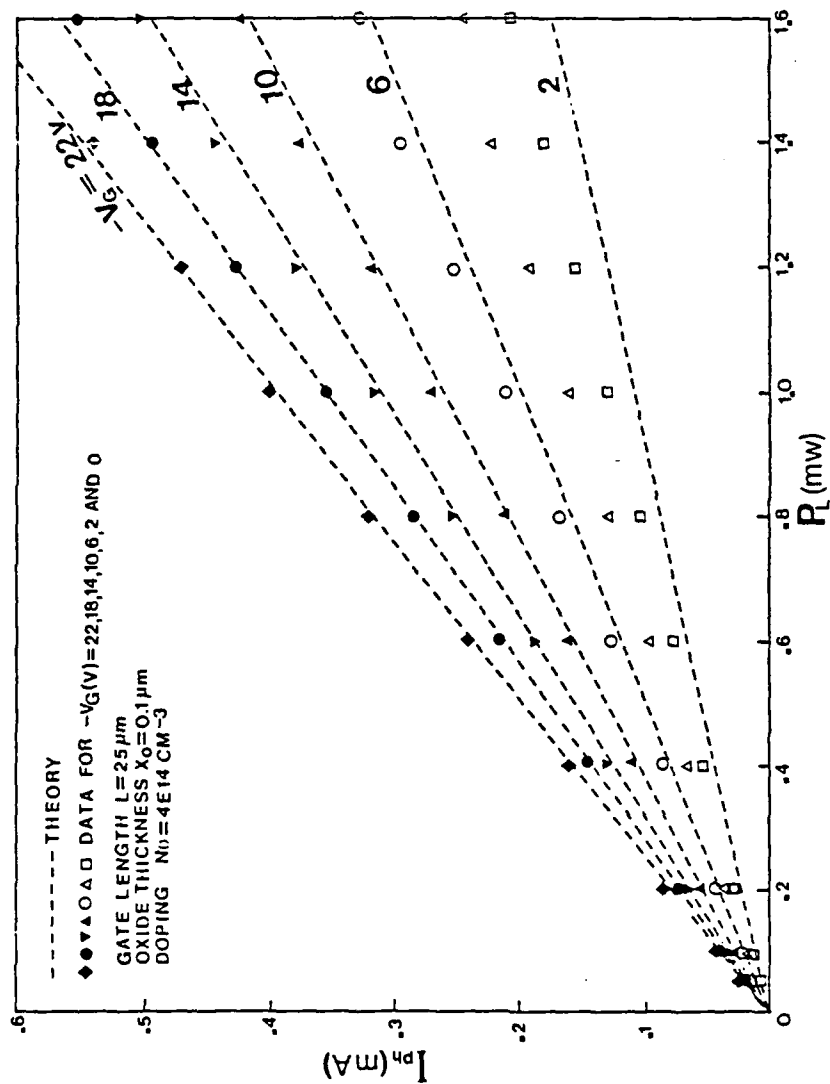


Fig. 7

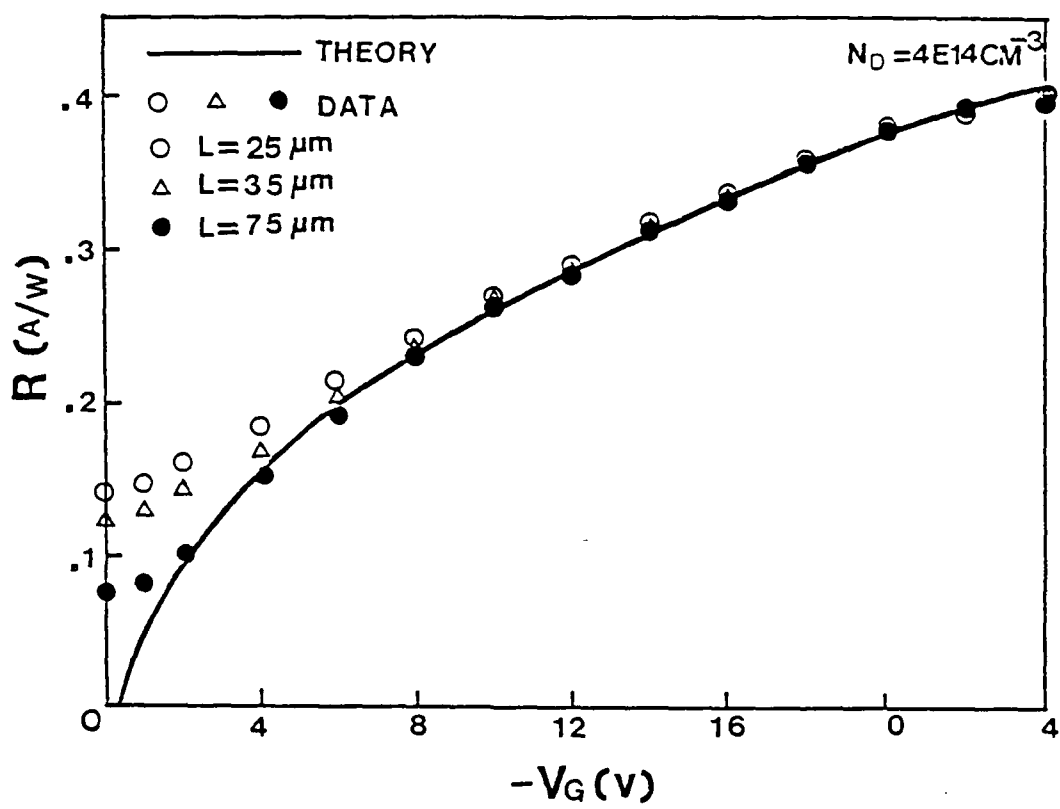


Fig. 8

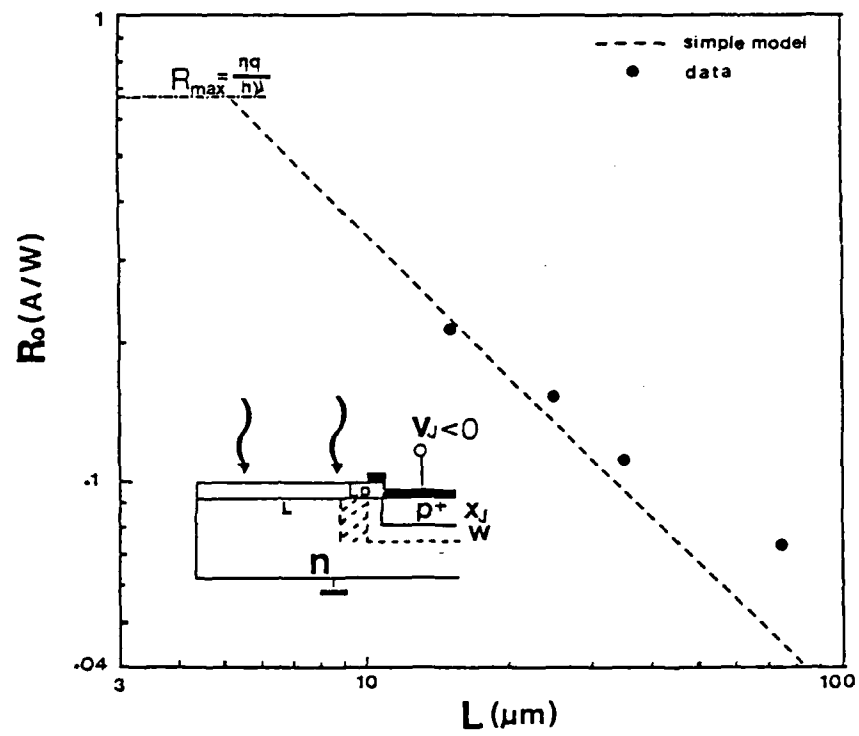


Fig. 9

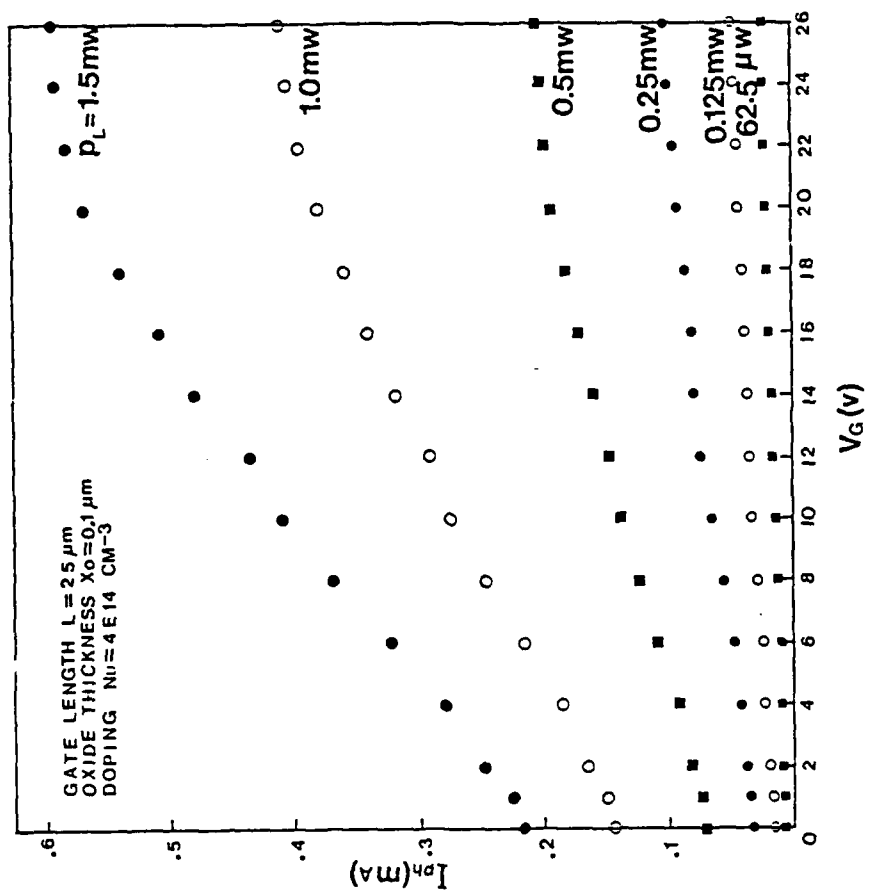


Fig. 10

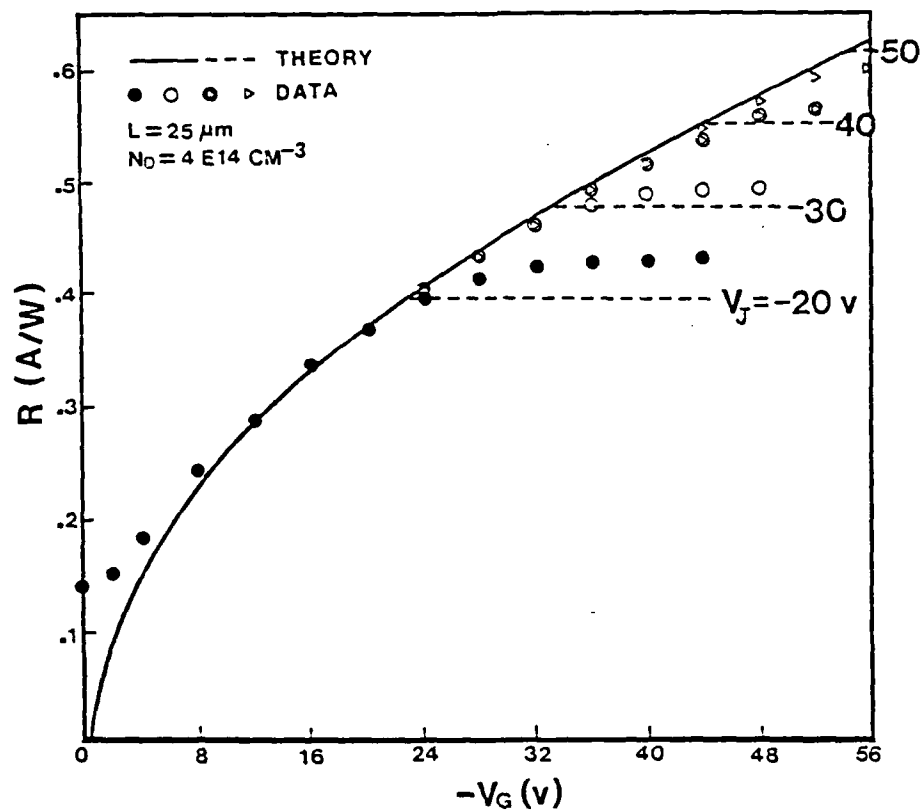


Fig. 11

$$\vec{Y} = \kappa \vec{A} \cdot \vec{X}$$

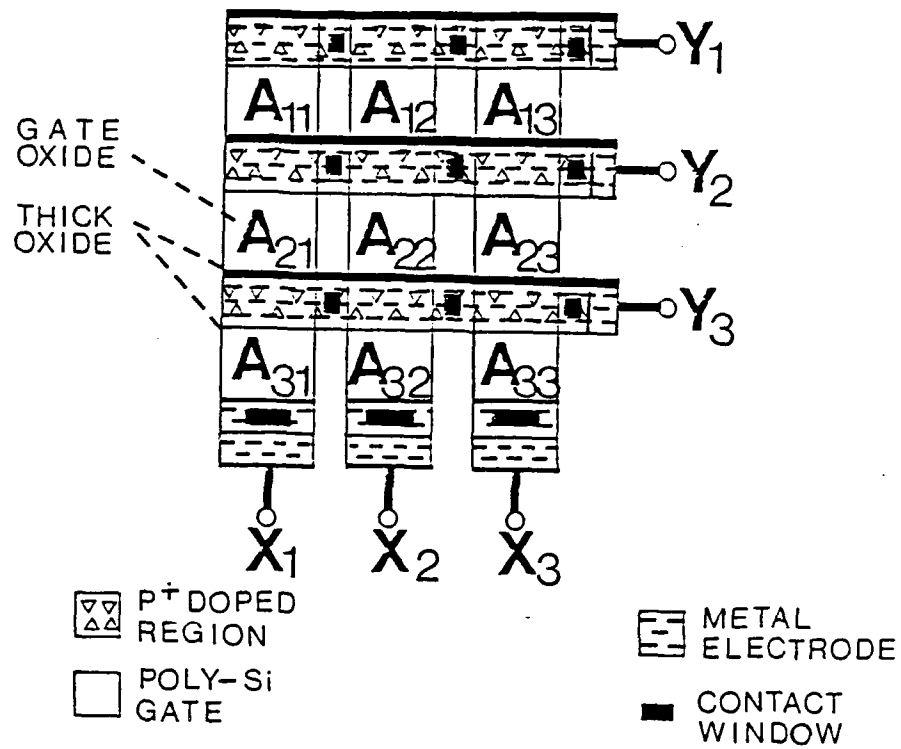


Fig.12